Hierarchical analysis and multi-scale modelling of rat cortical and trabecular bone

Ramin Oftadeh[1,2], Vahid Entezari[1], Guy Spörri[1,3], Juan C. Villa-Camacho[1], Henry Krigbaum[4], Elsa Strawich[5], Lila Graham[5], Christian Rey[6], Hank Chiu[7], Ralph Müller[3], Hamid Nayeb Hashemi[2], Ashkan Vaziri[2] and Ara Nazarian[1]

[1]Center for Advanced Orthopaedic Studies, Department of Orthopaedic Surgery, Beth Israel Deaconess Medical Center, Harvard Medical School, Boston, MA, USA
[2]Department of Mechanical and Industrial Engineering, Northeastern University, Boston, MA, USA
[3]Institute for Biomechanics, ETH Zurich, Zurich, Switzerland
[4]Department of Orthopaedics, University of California, San Francisco, CA, USA
[5]Laboratory for the Study of Skeletal Disorders and Rehabilitation, Boston Children's Hospital, Department of Orthopaedic Surgery, Harvard Medical School, Boston, MA, USA
[6]Centre Inter Universitaire de Recherche et d'Ingénierie des Matériaux, Ecole Nationale Supérieure des Ingénieurs en Arts Chimiques et Technologiques, Toulouse, France
[7]Department of Biomedical Engineering, University of Memphis, Memphis, TN, USA

The aim of this study was to explore the hierarchical arrangement of structural properties in cortical and trabecular bone and to determine a mathematical model that accurately predicts the tissue's mechanical properties as a function of these indices. By using a variety of analytical techniques, we were able to characterize the structural and compositional properties of cortical and trabecular bones, as well as to determine the suitable mathematical model to predict the tissue's mechanical properties using a continuum micromechanics approach. Our hierarchical analysis demonstrated that the differences between cortical and trabecular bone reside mainly at the micro- and ultrastructural levels. By gaining a better appreciation of the similarities and differences between the two bone types, we would be able to provide a better assessment and understanding of their individual roles, as well as their contribution to bone health overall.

Subject Areas:
biomechanics, biomedical engineering

Keywords:
cortical and trabecular bone, hierarchical analysis, continuum micromechanics, bone mechanical properties, bone composition and structure

Author for correspondence:
Ara Nazarian
e-mail: anazaria@bidmc.harvard.edu

1. Introduction

Cortical and trabecular bone are arranged within a hierarchical structure in the osseous tissue: this diversity of structures allows the skeleton to perform its mechanical and metabolic functions. Different factors, such as bone mass, geometry, material properties, cortical to trabecular proportion, molecular composition, microstructure and architecture, contribute to the tissue's strength and quality [1–3].

Collagen fibres, as an organic component, and carbonated apatite crystals, as a non-organic component, contribute to bone's strength by resistance against loads applied to its structure [1]. The mineral phase is the main determinant of stiffness, whereas collagen content governs its post-yield ductility. The mechanical properties of bone are ultimately determined by the mineral content and its distribution pattern within the collagenous matrix, as well as the tissue's structural, microstructural and nanostructural organization [4].

Composed primarily of osteons of concentric lamellae, cortical bone is remarkably stiff and contributes substantially to the tissue's mechanical strength. On the other hand, trabecular bone is arranged in a mosaic of angular segments of parallel sheets of lamellae and shows a greater rate of metabolic activity, lower modulus and larger surface-area-to-volume ratio [2,5–7].

Extensive research has been conducted to distinguish cortical from trabecular bone [4,7–30]. Although a variety of animal models and analytical techniques have been employed to assess the differences between these two

structural components—especially in the context of endocrine, dietary and stress variables—few studies have compared them in a comprehensive manner. Bigi *et al.* [13] have reported the CO_3 and Ca/P content of trabecular and cortical bone in mouse. Bagi *et al.* [15] analysed the yield load and stiffness of cortical bone in mouse based on bone volume fraction. Toolan *et al.* [31] analysed the effects of bisphosphonates on the mechanical behaviour of rat bones. Hodgskinson *et al.* [19] and Kuhn *et al.* [11] reported the hardness and Ca, CO_3, C/PO_4 and Ca/P content for trabecular and cortical bone of bovine. Limited data have been reported on pig and dog [22,32]. The majority of work on human contains mineral density, bone volume fraction, tissue modulus and module of elasticity [7,21,23–27,29,30]. These studies have produced inconsistent results and have only provided snapshots of the vast spectrum of data on which to base an exhaustive comparison (table 1).

Given the complex nature of bone, a comparison between its cortical and trabecular components should consider the hierarchical arrangement of structural properties for these two distinct tissues. Recent technological advancements have allowed researchers to evaluate bone's properties at ultra-, micro- and nanostructural levels, facilitating new insights into the tissue's material properties. Moreover, by considering the relative influences of certain structural parameters on bone strength and modulus, the tissue's mechanical properties can be predicted by mathematical modelling with single- and two-parameter power-law or linear functions [33–37]. However, owing to the heterogeneity and anisotropic material properties of cortical and trabecular bone, these methods cannot fully predict the mechanical properties of bone. In recent years, several methods have been proposed to overcome this shortcoming [38–43]. One of the methods considered for this purpose is the continuum micromechanics approach [44,45]. Continuum micromechanics is the analysis of heterogeneous or anisotropic materials at the level of the individual material elements forming these materials [44,45]. It has been used in several applications including modelling of defects in solids [46], mechanical properties of composites [47], electroelastic moduli of piezoelectric composites [48] and recently in modelling of mechanical properties of bone [40,42,43].

The aim of this study is to explore the hierarchical arrangement of structural properties in cortical and trabecular bone and to determine a mathematical model that accurately predicts the tissue's mechanical properties as a function of these indices (figure 1). By gaining a better appreciation of the similarities and differences between the two bone types, we will be able to provide a better assessment and understanding of their individual roles, as well as their contribution to bone health overall [11,18].

2. Material and methods

2.1. Specimen preparation

The study protocol was approved by the Institutional Animal Care and Use Committee at Beth Israel Deaconess Medical Center, Boston, MA. Thirty Sprague–Dawley female rats (20 weeks old) were obtained from Charles River Laboratories (Charlestown, MA, USA) and euthanized via CO_2 inhalation. Cylindrical samples of diaphyseal cortical bone (height 6.85 $\pm$ 0.85 mm) and distal metaphyseal trabecular bone (height 5.17 $\pm$ 0.65 mm) specimens were obtained from each femur (figure 2). Additionally, secondary specimens for embedding were obtained by cutting 1-mm-thick diaphyseal and distal metaphyseal sections from all femurs. The specimen preparation protocol has been published in detail elsewhere [49]. All specimens underwent cleaning via sonic agitation (Fisher Scientific International, Hampton, NH, USA) while suspended in distilled water for 20 min, followed by centrifugal removal of excess water and marrow at 9*g* for 15 min. The details of the analytical methods will be presented in hierarchical fashion as follows.

2.2. Macrostructural properties

2.2.1. Extrinsic structural properties

All cylindrical specimens underwent uniaxial compression (INSTRON 8511, Instron Corporation, Norwood, MA, USA) for determination of properties through analysis of the load–displacement curve. Structural stiffness was defined as the slope of the linear portion of the curve, whereas yield load was represented at the point where the curve ceased to be linear. The point with the highest load value represents the ultimate load.

2.2.2. Bone tissue density (ρ_t)

Bone mass and tissue volume (TV) of cylindrical specimens were measured by a precision scale (AnalyticalPlus, Ohaus, Pine Brook, NJ, USA) and gas pycnometry (AccuPyc 1330, Micromeritics, GA, USA). Bone tissue density was calculated by dividing bone mass by bone tissue volume.

2.2.3. Mineral and matrix content

In order to determine the mineral (ash mass/dry mass) and matrix (1 − (ash mass/dry mass)) contents, the cylindrical specimens were dried at 70°C for 24 h and ashed at 600°C for 96 h (Furnace 48000, Thermolyne, Dubuque, IA, USA). It has been shown that some parts of mineral evaporate at 600°C and quantitatively contribute to 6.6% of mineral weight. Therefore, the measured mineral content should be multiplied by 1.066 to show the actual mineral content in the bone.

2.3. Microstructural properties

2.3.1. Morphometric indices

Bone volume fraction (BV/TV) and bone-surface-to-volume ratio (BS/BV) of the trabecular and cortical cylindrical specimens were assessed using micro-computed tomography (μCT40; Scanco Medical AG, Brüttisellen, Switzerland—tube energy and current, 55 kVp and 145 μA, respectively; integration time, 250 ms; and isotropic voxel size, 20 μm).

2.3.2. Apparent material properties

Apparent mechanical properties were calculated from the stress–strain curves obtained from uniaxial compression testing. The minimum cross-sectional areas for cancellous and cortical bone specimens were calculated from μCT images (figure 3). The modulus of elasticity (E) was determined from the slope of the linear portion of the curve, while the point where the curve ceased to be linear was designated as the yield strength (YS). The point with the highest strength value represented the ultimate strength (US).

2.4. Nanostructural properties

2.4.1. Nanoindentation

The secondary specimens were dehydrated with ethyl alcohol, embedded in epoxy resin and polished. The midsections of the trabecular elements and the cortical shells were selected as indentation sites using a Berkovich indenter (Hysitron Triboindenter, Minneapolis, MN, USA) to avoid boundary condition errors. Thirty-five indentations distributed across the cross section of each sample were done and the results were averaged per sample.

Table 1. A chronological snapshot of comparative hierarchical properties of cortical and trabecular bones.

level	indices	ref.	bone type	testing technique	cortical bone	cancellous bone
macro-structure	ash (inorganic) content %	[13]	rat femur/tibia	thermogravimetry	66.4 (0.3)	62.0 (0.3)
		[21]	steer vertebra/tibia	gravimetry	67.86	64.55
	protein content (%)	[21]	steer vertebra/tibia	gravimetry	28	31.09
	bone mineral density (BMD) (g cm^{-3})	[17]	mouse femur/tibia	μCT	1.089 (0.017)	0.745 (0.102)
		[28]	human (black) tibia	peripheral QCT	0.229 (0.088)	1.188 (0.043)
			human (white) tibia		0.255 (0.053)	1.117 (3.6)
	bone tissue density (ρ_T) (g cm^{-3})	[22]	rat vertebra/femur	gravimetry	2.066 (0.005)	1.908 (0.011)
		[21]	human vertebra/tibia	gravimetry	1.91	1.87
			steer vertebra/tibia	gravimetry	1.995 (0.01)	1.93 (0.22)
	stiffness (N mm^{-1})	[15]	rat femoral midshaft	three-point bending	47.24 (6.59)	—
		[31]	rat femoral midshaft	three-point bending	588 (75)	—
			rat vertebra	compression	—	1327 (336)
	failure load (N)	[15]	rat femoral midshaft	three-point banding	160.09 (30.80)	—
microstructure	BV/TV (mm^3 mm^{-3})	[15]	rat femur	μCT	0.46	0.11 (0.04)
		[17]	mouse femur/tibia	μCT	—	0.25 (0.06)
		[20]	fetal pig mandibular	μCT	—	24.14 (4.14)
	mod. of elasticity (GPa)	[30]	human iliac crest (23 year)	three-point bending	3.76 (1.68)	3.03 (1.63)
			human iliac crest (63 year)	three-point bending	5.26 (2.09)	4.16 (2.02)
		[7]	human tibia	four-point bending	6.75 (1.00)	5.72 (1.27)
		[29]	human proximal tibia	three-point banding	5.44 (1.25)	4.59 (1.6)
	yield strength (YS) (GPa)	[27]	human femur	compression	0.109	0.089
nanostructure	tissue modulus (GPa)	[32]	porcine femur	microindentation	11.6 (9.5)	5.9 (4.3)
				nanoindentation	16.4 (1.3)	21.5 (2.1)
		[25]	human vertebrae/tibia	nanoindentation	25.8 (0.7)	13.4 (2.0)
		[26]	human femur	acoustic microscopy	17.73 (0.22)	17.5 (1.12)
				nanoindentation	20.02 (0.27)	18.14 (1.7)
		[4]	human femur	nanoindentation	21.2 (5.3)	11.4 (5.3)
	hardness (GPa)	[25]	human vertebrae/tibia	nanoindentation	0.736 (0.034)	0.468 (0.079)
		[4]	human femur	nanoindentation	0.234–0.76	0.234–0.76
composition	CO_3 (—)	[13]	rat femur/tibia	FT-IR	3.8 (0.2)	2.3 (0.2)
		[11]	bovine femur/tibia	chemical analysis	5.33 (0.1)	5.33 (0.18)
	C/PO_4 (—)	[11]	bovine femur/tibia	chemical analysis	0.17	0.17
	Ca (mg g^{-1})	[19]	bovine femur	colorimetry	271	257
		[23]	child vertebrae/femur	gravimetry	194	47.4
	HPO_4 (%)	[11]	bovine femur/tibia	FT-IR	20.3 (0.2)	20.7 (0.2)
	PO_4	[11]	bovine femur/tibia	FT-IR (%)	9.6 (0.1)	8.7 (0.1)
		[23]	child vertebrae/femur	chemical analysis (mg g^{-1} of bone)	24.1	90.3
	Ca/P (—)	[13]	rat femur/tibia	spectrophometry	1.63 (0.2)	1.5 (0.2)
		[11]	bovine femur/tibia	chemical analysis	1.64 (0.02)	1.58 (0.06)

2.5. Compositional properties

2.5.1. Total protein and collagen content

Following uniaxial compression testing, cylindrical specimens were subjected to amino acid analysis. For this purpose, specimens were powdered using a Spex mill (SPEX Freezer/Mill; SPEX Industries Inc., NJ, USA) and lyophilized to recover cortical and trabecular bone powder. The matrix analysis was performed with an amino acid analyser (Beckman System 7300; Beckman Coulter Inc., CA, USA). The amino acids were separated by ion-exchange chromatography followed by post-column derivatization using ninhydrin for detection. Signals at 440 and 570 nm wavelengths were

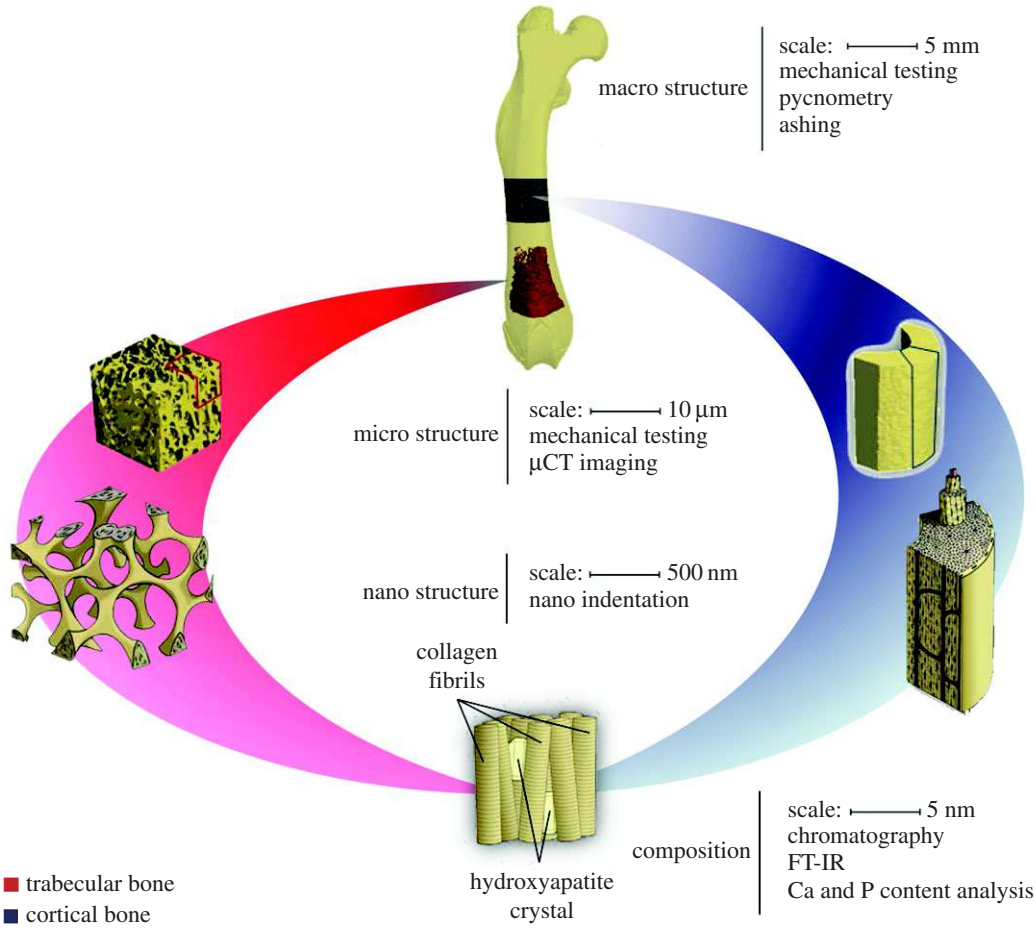

Figure 1. An illustration of the hierarchical nature of cortical and trabecular bone.

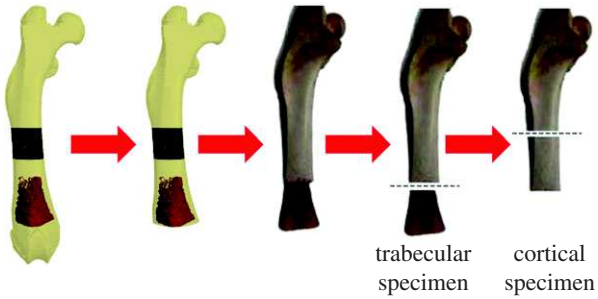

Figure 2. An illustration of the preparation process for cortical and trabecular specimens.

integrated, and the concentration of each ninhydrin-reactive component was recorded.

2.5.2. Phosphate (PO_4), hydrogen phosphate (HPO_4), carbonate (CO_3), carbonate/phosphate and protein/mineral content

Fourier transform infrared (FT-IR) spectroscopy was performed on cylindrical specimens using a spectrometer (Perkin-Elmer, Waltham, MA, USA). The spectra were curve-fitted in the ν_4 PO_4, ν_2 CO_3 and amide band domains (Galactic GRAMS Software, Salem, NH, USA). The ν_4 PO_4 domain shows five main phosphate bands at 600, 575 and 560 cm^{-1} for PO_4 groups in an apatite lattice, and 617 and 534 cm^{-1} for non-apatitic environments corresponding to surface location (figure 4*a*) [50]. The ν_2 CO_3 domain was decomposed into three bands at 879, 871 and 866 cm^{-1} related to types A and B carbonate, and carbonate ions in non-apatitic environments, respectively (figure 4*b*) [51]. The amide–ν_3 carbonate domain (1300–1800 cm^{-1}) was decomposed into seven bands at 1750, 1670, 1640, 1550, 1510, 1450 and 1410 cm^{-1}. The relative intensity of the mineral and protein bands has proven to be an accurate measure of the mineral-to-protein ratio [52].

2.5.3. Calcium and phosphate (PO_4) content

Calcium content was determined using an NBX electron microprobe (Cameca Instrument, Nampa, ID, USA) on isolated mineral crystals pressed into a flat pellet (beam voltage, 10 keV; beam current, 30 nA; and a rastered beam, 64 × 64 µm) [53,54]. On the other hand, a modified Fiske and Subbarow colorimetric method at the peak absorption of 660 µm was used to quantify the phosphate content [55–57].

2.6. Statistical analysis

Normality of continuous data was assessed by using the Kolmogorov–Smirnov test. Comparative analyses were performed by one-way analysis of variance (ANOVA), with bone type (cortical and trabecular) as independent variables, and outcome measures from different testing modalities as dependent variables. In addition, a regression analysis was conducted to determine the correlation between axial stiffness derived from experiments and that derived from the micromechanics model. Statistical analysis was performed using the PSAW software package (version 19.0; SPSS Inc./IBM, Chicago, IL, USA). Two-tailed values of $p < 0.05$ were considered statistically significant.

2.7. Mathematical modelling

Bone has a hierarchical structure [58,59]; therefore, each level of hierarchy plays a significant role in the mechanical properties of bone structure. Figure 5 shows the four levels of hierarchy inspired from material composition and structure of the bone: nanoscale (10–100 nm), submicroscale (1–10 µm), microscale

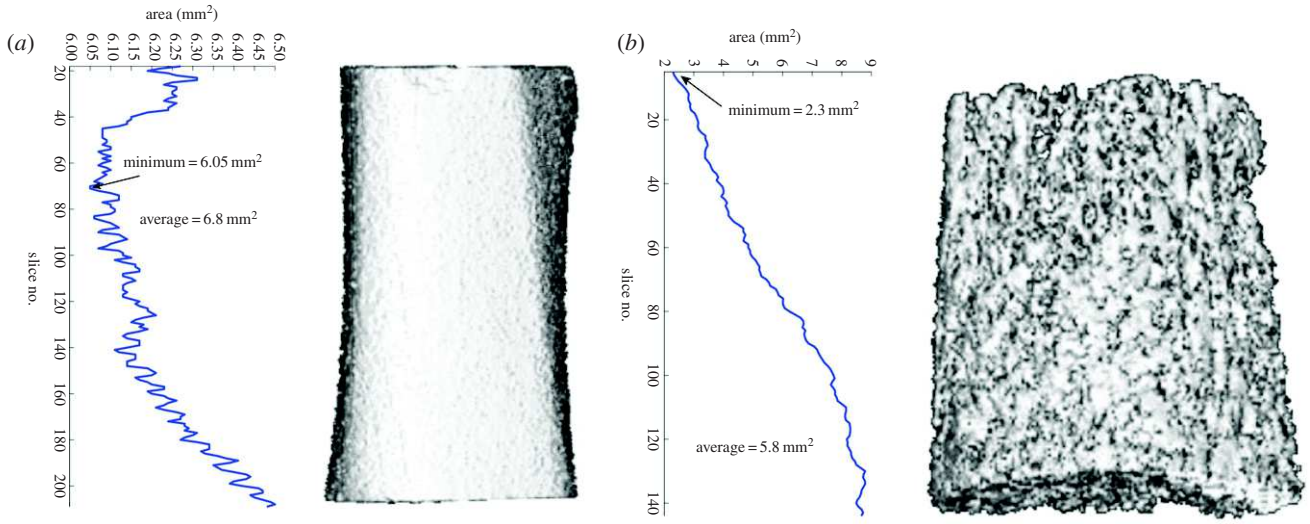

Figure 3. Calculation of minimum cross-sectional area for (*a*) cortical and (*b*) trabecular specimens. (Online version in colour.)

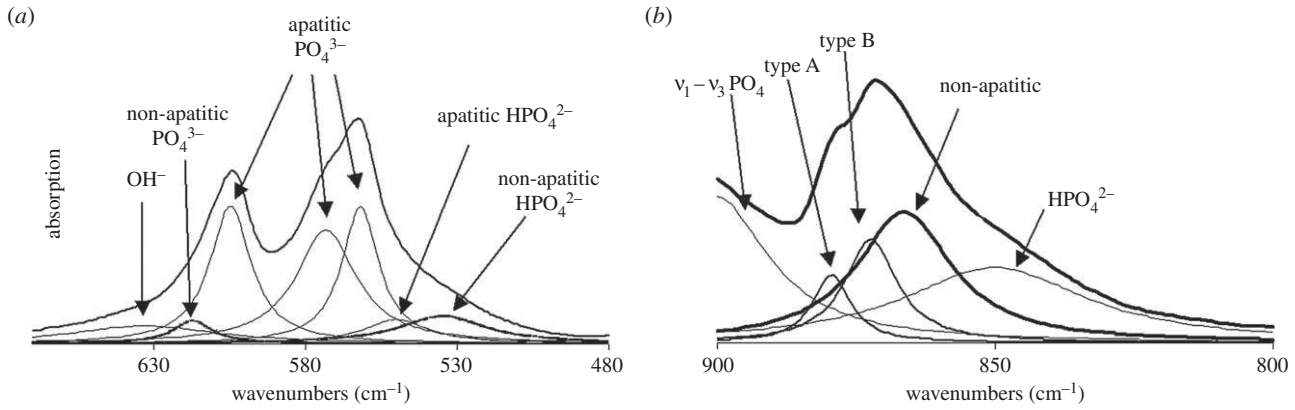

Figure 4. (*a*) Infrared spectrum in the ν_4 PO_4 domain of a synthetic nanocrystalline apatite (maturation time 3 days, exempt of foreign ions). Curve-fitting (Lorentzian band shape) showing the different absorption bands and their attribution. (*b*) Infrared spectrum in the ν_2 CO_3 domain of a synthetic nanocrystalline apatite (maturation time 3 days, prepared in the presence of carbonate ions). Curve-fitting (Lorentzian band shape) showing the different absorption bands and their attribution.

(10–100 μm) and macroscale (0.5–10 mm). The objective of mathematical modelling is to relate macrostructural mechanical properties of bone to its elementary components, namely hydroxyapatite (HA) crystals, collagen, non-collagenous proteins (NCPs) and water.

A micromechanics approach is ideal for modelling the mechanical properties of bone owing to the tissue's heterogeneity and complex structure. The basic concept behind it is to hierarchically label the representative volume elements (RVEs) in the bone structure. Based on the micromechanics approach framework, the RVEs should have two main aspects: first, the characteristic dimension of these volume elements (l) should be considerably larger than the characteristic length (d) of the elements constructing them and at the same time extremely smaller than the characteristic dimensions (L) of the architecture built by the RVEs (i.e. $d \ll l \ll L$). Second is the ability of RVEs to be divided into phases with constant material properties.

At each level of hierarchy, the phases and their properties are defined (volume fractions ϕ and elastic stiffnesses $\mathbf{c}$). Based on the linear elasticity estimate of continuum micromechanics and assuming constant elastic modulus for the phases in the RVEs, the homogenized stiffness of RVEs, $\mathbf{C}^0_{\text{est}}$, can be determined as [44,45]

$$\mathbf{C}^0_{\text{est}} = \sum_{r=1}^{n} \phi_r \mathbf{c}_r : (\mathbf{I} + \mathbf{P}^0_r : (\mathbf{c}_r - \mathbf{C}^0))^{-1} : \left[\sum_{s=1}^{n} \phi_s (\mathbf{I} + \mathbf{P}^0_s : (\mathbf{c}_s - \mathbf{C}^0))^{-1} \right]^{-1}, \tag{2.1}$$

where n is the number of phases in the RVEs, $\mathbf{c}$ is the phase stiffness, $\mathbf{I}$ is the fourth-order unity tensor and $\mathbf{C}^0$ is the homogeneous elastic matrix stiffness which is included in the phases. Tensor $\mathbf{P}^0$ is related to the Eshelby tensor [60] ($\mathbf{P}^0 = \mathbf{S}^{0\text{Esh}} : \mathbf{C}^{0,-1}$), which characterizes the interaction between phases in the RVEs.

In micromechanics modelling, the elastic stiffness of RVEs found in each level of hierarchy will be used as phase stiffness for the analysis of subsequent levels. There are several estimates in the literature for choosing $\mathbf{C}^0$. The Mori–Tanka scheme [61,62] is the model which chooses $\mathbf{C}^0 = \mathbf{C}^{\text{matrix}}$, meaning that there is an inclusion phase consisting of small particles embedded in the continuous-matrix phase. This model, which is best suited for particle-reinforced composites, has an explicit solution. The self-consistent scheme [63,64] is the model which chooses $\mathbf{C}^0 = \mathbf{C}^0_{\text{est}}$, meaning that the phases are dispersed with the stiffness properties of homogenized RVEs. For the self-consistent scheme, equation (2.1) is reduced to a set of nonlinear equations. Here, the micromechanics representation of each phase and corresponding elastic modulus tensors are derived.

2.7.1. Nanoscale

2.7.1.1. Interaction of water and non-collagenous proteins with hydroxyapatite

At the nanostructural level, HA crystals, water and NCPs (figure 5) interact with each other. At this level, phases are

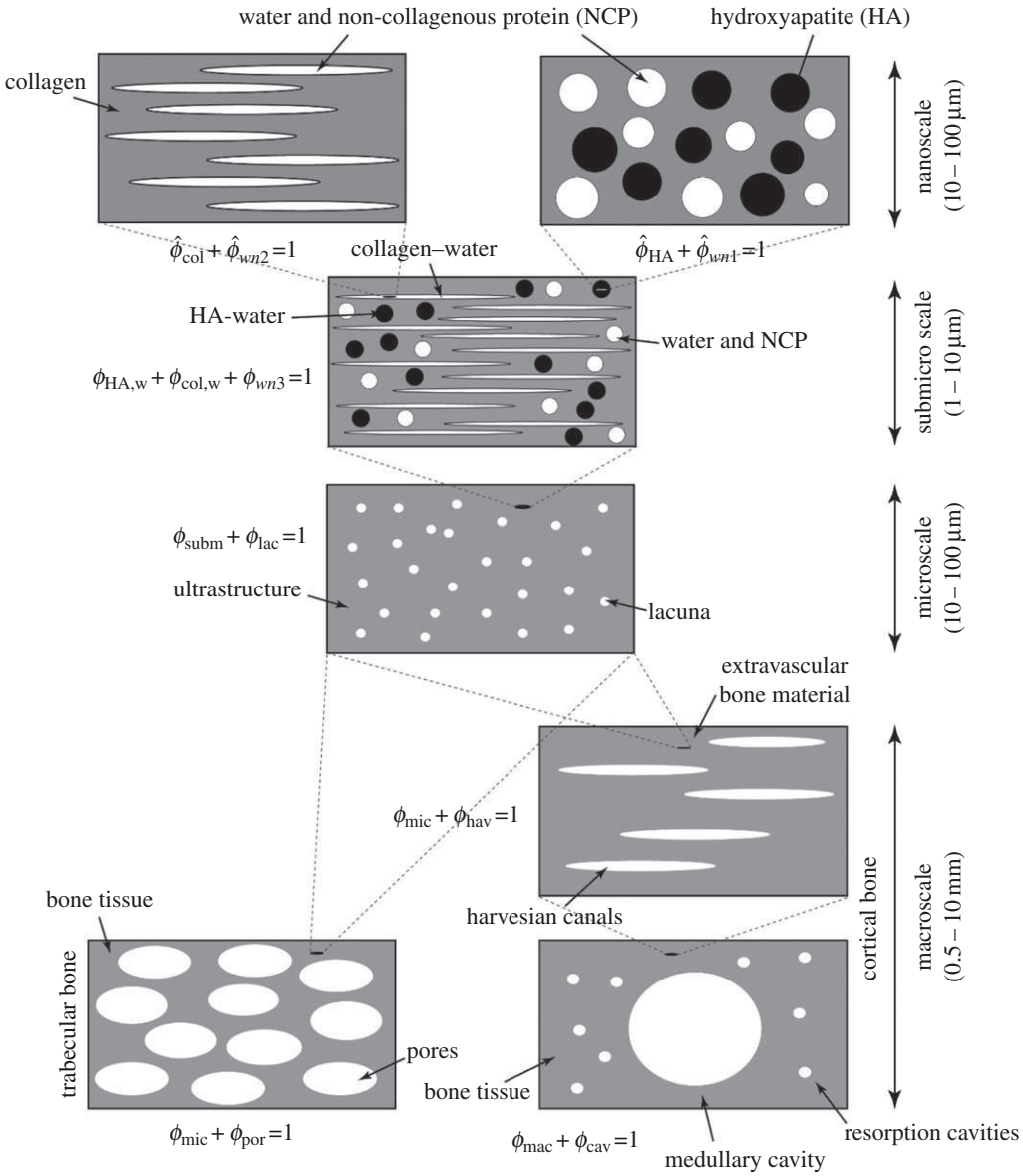

Figure 5. Micromechanics representation of hierarchical structure of bone with four levels of hierarchy from nano- to macroscale.

dispersed, thus warranting the use of a self-consistent scheme

$$\mathbf{C}_{HA,w} = \sum_{r=1}^{n} \hat{\phi}_r \mathbf{c}_r : (\mathbf{I} + \mathbf{P}_r : (\mathbf{c}_r - \mathbf{C}_{HA,w}))^{-1} : \left[\sum_{s=1}^{n} \hat{\phi}_s (\mathbf{I} + \mathbf{P}_s : (\mathbf{c}_s - \mathbf{C}_{HA,w}))^{-1} \right]^{-1}. \quad (2.2)$$

HA minerals are platelet shaped [65–68], and water is considered to have a spherical shape. Volume fractions of HA and water are $\hat{\phi}_{HA}$ and $\hat{\phi}_{wn1}$, with a sum equal to 1,

$$\hat{\phi}_{HA} + \hat{\phi}_{wn1} = 1. \quad (2.3)$$

Platelet-shaped HA minerals make the RVE matrix anisotropic. Using Laws formula [69,70] for determining the **P** tensor in a transversely isotropic matrix, the **P** tensor can be found for water and HA (appendix A.1). Assuming isotropic material properties for water and HA, the corresponding elastic matrices can be written as

$$\mathbf{c}_{HA} = 3K_{HA}\mathbf{I}^{vol} + 2G_{HA}\mathbf{I}^{dev} \quad (2.4)$$

and

$$\mathbf{c}_{wn1} = 3K_{w}\mathbf{I}^{vol} + 2G_{w}\mathbf{I}^{dev}, \quad (2.5)$$

where K_{HA}, G_{HA}, K_w and G_w are the isotropic stiffness properties of the HA and water. $\mathbf{I}^{vol}$ and $\mathbf{I}^{dev}$ are, respectively, the volumetric and deviatoric part of the fourth-order unity tensor ($\mathbf{I}^{vol} = 1/3\delta_{ij}\delta_{kl}$ and $\mathbf{I}^{dev} = \mathbf{I} - \mathbf{I}^{vol}$). For highly mineralized tissues, radial stiffness was shown to be equal to axial stiffness [71], which means that HA isotropically contributes to the bone tissue stiffness. For the exploration of the volume fraction–radial stiffness relation to the point where the volume fraction of HA is equal to 1, the isotropic elastic stiffness of HA is equal to 100 GPa. Based on the relation: $C_{11,HA} = E_{HA}(1 - \upsilon_{HA})/((1 + \upsilon_{HA})(1-2\upsilon_{HA}))$ and assuming $\upsilon_{HA} = 0.27$ [72], the elastic modulus, bulk modulus and shear modulus of HA can be found as 79.76, 57.8 and 31.4 GPa, respectively (table 2). Equation (2.2) leads to five coupled nonlinear equations, which should solve simultaneously to reach five constants of the transversely isotropic matrix $\mathbf{C}_{HA,w}$.

2.7.1.2. Interaction of water and non-collagenous proteins with collagen

At this level, fibrillar collagen molecules are attached to each other, and the space between them is filled with water and NCPs. Considering collagen molecules as a matrix and the interspace water and NCPs as an inclusion, from the Mori–Tanaka scheme, the corresponding stiffness can be written as

$$\mathbf{C}_{col,w} = [\hat{\phi}_{col}\mathbf{c}_{col} + \hat{\phi}_{wn2}\mathbf{c}_{wn2} : (\mathbf{I} + \mathbf{P}_{wn2} : (\mathbf{c}_w - \mathbf{c}_{col}))^{-1}] : [\hat{\phi}_{col}\mathbf{I} + \hat{\phi}_{wn2}(\mathbf{I} + \mathbf{P}_{wn2} : (\mathbf{c}_w - \mathbf{c}_{col}))^{-1}]^{-1}. \quad (2.6)$$

Table 2. Isotropic mechanical properties of bone elementary components.

component	elastic modulus[a] (Gpa)	Poisson's ratio (v)	bulk modulus, K (GPa)	shear modulus, G (GPa)	reference
hydroxyapatite	79.76	0.27	57.8	31.4	[71]
collagen	5.4	0.28	4.1	2.1	[73]
water and non-collagenous protein	0	0.49	2.3	0	

[a]Only two of these parameters are independent. The other two can be found based on universal relations for isotropic material.

Assuming isotropic material properties for the collagen matrix, the corresponding elastic modulus matrix can be written as

$$\mathbf{c}_{\text{col}} = 3K_{\text{col}}\mathbf{I}^{\text{vol}} + 2G_{\text{col}}\mathbf{I}^{\text{dev}}, \tag{2.7}$$

where K_{col} and G_{col} are, respectively, the bulk modulus and shear modulus of the collagen stiffness matrix (table 2). Because the matrix is isotropic, the $\mathbf{P}_{\text{col}}$ tensor is defined based on the cylindrical inclusions embedded in an isotropic matrix (appendix A.2). Volume fractions of phases are $\hat{\phi}_{\text{col}}$ and $\hat{\phi}_{wn2}$ for collagen and water, respectively, where

$$\hat{\phi}_{\text{col}} + \hat{\phi}_{wn2} = 1. \tag{2.8}$$

2.7.2. Submicroscale

At this level, the organic and mineral phases interact with water and with each other. Stiffness matrices of mineral and organic phases come from RVEs at the nanolevel. Dispersion of the phases in the RVEs warrants the use of a self-consistent scheme:

$$\mathbf{C}_{\text{subm}} = \sum_{r=1}^{n} \phi_{\text{r}}\mathbf{c}_{\text{r}}:(\mathbf{I} + \mathbf{P}_{\text{r}}:(\mathbf{c}_{\text{r}} - \mathbf{C}_{\text{subm}}))^{-1}: \left[\sum_{s=1}^{n} \phi_{\text{s}}(\mathbf{I} + \mathbf{P}_{\text{s}}:(\mathbf{c}_{\text{s}} - \mathbf{C}_{\text{subm}}))^{-1}\right]^{-1}, \tag{2.9}$$

where $\mathbf{C}_{\text{subm}}$ is the stiffness of submicroscale. Volume fractions of phases occupying the RVEs are $\phi_{\text{HA},w}$, $\phi_{\text{col},w}$ and ϕ_{wn3}, where

$$\phi_{\text{HA,w}} + \phi_{\text{col,w}} + \phi_{wn3} = 1\ . \tag{2.10}$$

Spherical phase inclusions are chosen for mineral and water phases (i.e. $\mathbf{P}_{\text{min}} = \mathbf{P}_{\text{w}} = \mathbf{P}_{\text{sph}}$) and cylindrical phase inclusions are chosen for organic phases (i.e. $\mathbf{P}_{\text{mat}} = \mathbf{P}_{\text{cyl}}$; appendix A.1).

2.7.3. Microscale

At a microstructural level, lacunae containing osteocytes are enclosed by the continuous bone matrix. From the Mori–Tanaka scheme, considering the bone material as a matrix and lacunae as spherical inclusions with volume fractions of ϕ_{subm} and ϕ_{lac}, the stiffness of bone material at the microscale, $\mathbf{C}_{\text{mic}}$, becomes

$$\mathbf{C}_{\text{mic}} = [\phi_{\text{subm}}\mathbf{c}_{\text{subm}} + \phi_{\text{lac}}\mathbf{c}_{\text{lac}}:(\mathbf{I} + \mathbf{P}_{\text{lac}}:(\mathbf{c}_{\text{lac}} - \mathbf{c}_{\text{subm}}))^{-1}]: [\phi_{\text{subm}}\mathbf{I} + \phi_{\text{lac}}(\mathbf{I} + \mathbf{P}_{\text{lac}}:(\mathbf{c}_{\text{lac}} - \mathbf{c}_{\text{subm}}))^{-1}]^{-1}, \tag{2.11}$$

where $\mathbf{c}_{\text{lac}} = 3K_w\mathbf{I}^{\text{vol}} + 2G_w\mathbf{I}^{\text{dev}}$, $\mathbf{P}_{\text{lac}} = \mathbf{P}_{\text{sph}}$ for a transversely isotropic matrix and

$$\phi_{\text{subm}} + \phi_{\text{lac}} = 1. \tag{2.12}$$

The non-zero terms of $\mathbf{P}_{\text{lac}}$ are presented in appendix A.1.

2.7.4. Macroscale

The structure of cortical and trabecular bone becomes different at this level. Therefore, the modelling has been divided into cortical and trabecular bone (figure 5). The Haversian canals contain blood vessels and nerve cells; therefore, it is reasonable to assign water stiffness to them ($\mathbf{c}_{\text{hav}} = 3K_w\mathbf{I}^{\text{vol}} + 2G_w\mathbf{I}^{\text{dev}}$). The volume fractions of phases in the RVEs are ϕ_{hav} and ϕ_{mic}, where

$$\phi_{\text{hav}} + \phi_{\text{mic}} = 1. \tag{2.13}$$

For cortical bone, considering bone microstructure as a matrix and Haversian canals as inclusions and using the Mori–Tanaka scheme, the stiffness matrix can be written as

$$\mathbf{C}_{\text{mac}} = [\phi_{\text{mic}}\mathbf{c}_{\text{mic}} + \phi_{\text{hav}}\mathbf{c}_{\text{hav}}:(\mathbf{I} + \mathbf{P}_{\text{hav}}:(\mathbf{c}_{\text{hav}} - \mathbf{c}_{\text{mic}}))^{-1}]: [\phi_{\text{mic}}\mathbf{I} + \phi_{\text{hav}}(\mathbf{I} + \mathbf{P}_{\text{hav}}:(\mathbf{c}_{\text{hav}} - \mathbf{c}_{\text{mic}}))^{-1}]^{-1}. \tag{2.14}$$

Finally, to model the stiffness of trabecular and cortical bone structure ($\mathbf{C}_{\text{bone}}$), porosities in trabecular bone have considered as spherical inclusions, and medullary cavity and restoration cavities in cortical bone have been considered as cylindrical inclusions in a transversely isotropic matrix ($\mathbf{P}_{\text{por}} = \mathbf{P}_{\text{sph}}$, $\mathbf{P}_{\text{cav}} = \mathbf{P}_{\text{cyl}}$). Because porosities and cavities are vacant, their stiffnesses are set to zero ($\mathbf{c}_{\text{por}} = \mathbf{c}_{\text{cav}} = 0$). Using the Mori–Tanaka scheme, from equation (2.1) $\mathbf{C}_{\text{bone}}$ can be written as

$$\mathbf{C}_{\text{bone}} = [\phi_{\text{M}}\mathbf{c}_{\text{M}} + \phi_{\text{N}}\mathbf{c}_{\text{N}}:(\mathbf{I} + \mathbf{P}_{\text{N}}:(\mathbf{c}_{\text{N}} - \mathbf{c}_{\text{M}}))^{-1}]: [\phi_{\text{M}}\mathbf{I} + \phi_{\text{N}}(\mathbf{I} + \mathbf{P}_{\text{N}}:(\mathbf{c}_{\text{N}} - \mathbf{c}_{\text{M}}))^{-1}]^{-1} \tag{2.15}$$

and

$$\phi_M + \phi_N = 1, \tag{2.16}$$

where subscript M stands for mac and mic and subscript N stands for cav and por regarding cortical and trabecular bone, respectively.

2.7.5. Elementary-phase stiffness values and modelling parameters

Having a micromechanics model in hand, the elementary-phase stiffness values of the bone structure should be determined (i.e. K_{HA}, G_{HA}, K_{col}, G_{col}, K_w, G_w,). Table 2 shows the values which are chosen for the model. The phase stiffness matrices can be built based on these properties ($\mathbf{c}_{\text{HA}}$, $\mathbf{c}_{\text{col}}$, $\mathbf{c}_{\text{w}}$). Then, the tissue-specific composition data should be determined: $\hat{\phi}_{\text{col}}$, $\hat{\phi}_{wn1}$, $\hat{\phi}_{\text{HA}}$ and $\hat{\phi}_{wn2}$ for nanoscale; $\phi_{\text{HA},w}$, $\phi_{\text{col},w}$ and ϕ_{wn3} for submicroscale; ϕ_{subm} and ϕ_{lac} for microscale; and ϕ_{mic}, ϕ_{hav}, ϕ_{mac}, ϕ_{cav} (cortical bone), ϕ_{por}, ϕ_{mic} (trabecular bone) for macroscale.

First, the volume fractions of bone elementary components ϕ_{col}, ϕ_{HA} and ϕ_{wn} are determined from experimental data. Having mineral density ($\rho^*_{\text{min}} = m_{\text{min}}/V_{\text{bone}}$) as a ratio of mineral mass m_{min} to bone volume V_{bone}, found from μCT analysis (table 3) and the mass density of HA as $\rho_{\text{HA}} = 3\ \text{g cm}^{-3}$ [74] the volume fraction of HA can be obtained as

$$\phi_{\text{HA}} = \phi_{\text{min}} = \frac{\rho^*_{\text{min}}}{\rho_{\text{HA}}}. \tag{2.17}$$

Bone mineral content (BMC), which is the ratio of mineral mass (m_{min}) over dry bone mass (m_{dry}), is determined using ashing

Table 3. Composition and axial module of elasticity of cortical and trabecular bone.

structure	BV/TV (Φ_{bone})	mineral density (mg cm^{-3})	Φ_{HA} (equation (2.17))	Φ_{col} (equation (2.18))	E_{exp} (MPa)
cort.	0.681	1031.404	0.344	0.363	11 547.87
cort.	0.582	1039.963	0.347	0.39	6807.52
cort.	0.502	1023.679	0.341	0.361	3681.35
cort.	0.539	991.172	0.33	0.261	6882.1
cort.	0.593	1035.283	0.345	0.331	6558.1
cort.	0.533	1024.222	0.341	0.363	4533.97
cort.	0.71	1033.027	0.344	0.335	11 201.11
cort.	0.714	1008.662	0.336	0.267	9516.63
cort.	0.68	1016.562	0.339	0.3	10 884.01
cort.	0.682	1013.443	0.338	0.295	9975.74
cort.	0.628	1008.42	0.336	0.277	10 449.87
cort.	0.626	1003.777	0.335	0.27	9012.52
cort.	0.543	1048.647	0.35	0.328	4197.04
cort.	0.53	1024.542	0.342	0.36	5574.04
cort.	0.723	1053.653	0.351	0.282	10 903.1
cort.	0.642	1033.69	0.345	0.332	11 500.08
cort.	0.698	1025.488	0.342	0.356	11 729.17
cort.	0.699	1062.7	0.354	0.284	9000.9
cort.	0.576	1009.146	0.336	0.289	5197.7
cort.	0.578	1020	0.34	0.315	7664.45
trab.	0.444	789.609	0.263	0.218	2982.19
trab.	0.451	786.057	0.262	0.211	2243.71
trab.	0.509	709.283	0.236	0.194	2482.5
trab.	0.536	753.249	0.251	0.205	6346.28
trab.	0.443	682.138	0.227	0.155	3186.72
trab.	0.483	696.437	0.232	0.185	814.56
trab.	0.452	657.295	0.219	0.173	3184.05
trab.	0.533	651.083	0.217	0.218	5576.47
trab.	0.391	598.734	0.2	0.344	698.32
trab.	0.375	591.434	0.197	0.189	598.32
trab.	0.485	617.37	0.206	0.118	341.62
trab.	0.455	671.77	0.224	0.163	828.85
trab.	0.548	685.158	0.228	0.16	871.05
trab.	0.444	685.957	0.229	0.169	2396.38
trab.	0.414	618.033	0.206	0.182	3866.67
trab.	0.449	615.078	0.205	0.155	3264.69
trab.	0.496	688.174	0.229	0.177	4191.65
trab.	0.472	659.889	0.22	0.164	2884.53
trab.	0.368	631.535	0.211	0.196	1707.21
trab.	0.458	598.071	0.199	0.334	915.11

analysis). Taking the mass density of organic matrix as $\rho_{org} \approx \rho_{col} = 1.41$ g cm^{-3} [74,75], ϕ_{org} reads as

$$\phi_{org} = \left(\frac{1 - \mathrm{BMC}}{\mathrm{BMC}}\right)\frac{\rho_{HA}}{\rho_{org}}\phi_{HA}. \tag{2.18}$$

Here, the mass densities of protein and collagen are assumed to be the same. Approximately 90% of the mass density of protein is collagen [59,74], therefore $\phi_{col} = 0.9\phi_{org}$ (table 3). Then, the volume fraction of water and non-collagenous protein can readily be found as

$$\phi_{wn} = 1 - \phi_{col} - \phi_{HA}. \tag{2.19}$$

Table 4. Macro-, micro-, nano- and compositional-level properties of rat cortical and trabecular bone found by this study.

variable	modality	units	cortical bone	cancellous bone	*p* value
bone tissue density	pycnometry	g cm^{-3}	2.17 (0.017)	2.16 (0.07)	0.78
mineral content	gravimetry	%	66.63 (7.64)	68.90 (9.94)	0.42
matrix content	gravimetry	%	28.97 (7.64)	26.55 (9.93)	0.42
stiffness	mechanical testing	N mm^{-1}	7199 (270)	719 (68)	<0.001
yield load	mechanical testing	N	737 (110)	43 (23)	<0.001
bone volume fraction	μCT imaging	mm^3 mm^{-3}	0.59 (0.03)	0.37 (0.04)	<0.001
bone-surface-to-volume ratio	μCT imaging	mm^2 mm^{-3}	3.84 (0.19)	14.44 (2.91)	<0.001
modulus of elasticity (*E*)	mechanical testing	GPa	8.50 (2.86)	2.47 (1.68)	<0.001
yield strength (YS)	mechanical testing	GPa	0.13 (0.02)	0.03 (0.01)	<0.001
tissue modulus	nano-indentation	GPa	18.98 (5.73)	18.27 (3.77)	0.46
hardness	nano-indentation	GPa	0.74 (0.25)	0.73 (0.21)	0.72
total protein	amino acid analysis	%	11.80 (4.11)	11.57 (3.43)	0.90
total collagen	amino acid analysis	%	10.50 (3.84)	9.58 (3.27)	0.59
collagen content in protein	amino acid analysis	%	88.57 (2.04)	82.04 (3.20)	<0.001
PO_4 (non-apatitic)	FT-IR	%	10.42 (1.95)	9.52 (1.30)	0.25
HPO_4	FT-IR	%	30.60 (4.74)	28.91 (4.80)	0.44
CO_3	FT-IR	%	3.63 (1.48)	2.56 (1.12)	0.11
C/P	FT-IR	—	0.056 (0.002)	0.058 (0.003)	0.09
protein-to-mineral ratio	FT-IR	—	0.77 (0.09)	0.70 (0.05)	0.89
Ca content	chemical analysis	μg mg^{-1} of bone	261.19 (100.40)	298.61 (20.135)	0.29
PO_4 content	chemical analysis	μg mg^{-1} of bone	18.74 (5.46)	19.26 (4.23)	0.76

The total volume fraction of water and non-collagenous proteins can be written as

$$\phi_{wn} = \hat{\phi}_{wn1} \times \phi_{\mathrm{col},w} + \hat{\phi}_{wn2} \times \phi_{\mathrm{HA},w} + \phi_{wn3}. \tag{2.20}$$

At nanoscale observation, volume fractions of HA and collagen ($\hat{\phi}_{\mathrm{HA}}$ and $\hat{\phi}_{\mathrm{col}}$) can be found as

$$\hat{\phi}_{\mathrm{col}} = \frac{\phi_{\mathrm{col}}}{\phi_{\mathrm{col},w}} \tag{2.21}$$

and

$$\hat{\phi}_{\mathrm{HA}} = \frac{\phi_{\mathrm{HA}}}{\phi_{\mathrm{HA},w}}. \tag{2.22}$$

Using equations (2.3), (2.8), (2.10), (2.20), (2.21) and (2.22) and assuming water contents in the two considered RVEs at the nano-level are the same ($\hat{\phi}_{wn1} = \hat{\phi}_{wn2}$), and also the water contents at the nano- and microlevels are equal ($\phi_{wn3} = \phi_{wn}/2$), the volume fraction composition at the nano- and submicroscale can be found as

$$\hat{\phi}_{wn1} = \hat{\phi}_{wn2} = \frac{\phi_{wn}}{2 - \phi_{wn}}, \tag{2.23}$$

$$\phi_{\mathrm{col},w} = \frac{2 - \phi_{wn}}{2 - 2\phi_{wn}} \phi_{\mathrm{col}} \tag{2.24}$$

and

$$\phi_{\mathrm{HA},w} = \frac{2 - \phi_{wn}}{2 - 2\phi_{wn}} \phi_{\mathrm{HA}}. \tag{2.25}$$

At the microlevel, the volume fraction of the lacunae is defined as the area of lacunae in the examined area divided by the total area. Here, ϕ_{lac} is assumed to be 2% [76–78]. The volume fraction of Haversian canals is defined as the ratio of the area of Haversian canals to the total considered area. ϕ_{hav} varies from 2% to 5% for healthy cortical bone [79], and here it is assumed to be 3% [80]. At last, for determining the volume fraction at the macrolevel (cortical and trabecular bone), ϕ_{mac} (cortical) and ϕ_{mic} (trabecular) are assumed to be equal to bone volume fraction (BV/TV). The experimental data for bone volume fraction can be found in table 3.

2.8. Finite-element analysis

μCT-based finite-element analysis was performed, for both trabecular and cortical bone, to evaluate the proposed micromechanics model. The models were meshed with eight-node linear hexahedral elements. The material was assumed to be linear elastic with the elastic modulus taken from experimental tissue modulus results for each sample (table 4). The number of elements ranged from 110 000 to 630 000 for trabecular samples and from 990 000 to 1 900 000 for cortical bone samples. To mimic the mechanical testing conditions, the lower surface of the models was fixed, whereas a linear displacement load was applied at the upper surface of the model. Then, the reaction forces at the superior surfaces were evaluated to determine the apparent elastic modulus of the samples.

3. Results

At the macrostructural level, no differences were observed between cortical and trabecular bone regarding tissue density (ρ_t), as measured by gravimetric methods ($p = 0.78$), and mineral and matrix contents, as assessed by ash content ($p = 0.42$ and 0.41, respectively). Nonetheless, stiffness and yield load values were significantly greater in cortical bone ($p < 0.001$ for both cases; table 4).

Cortical bone has a larger volume fraction ($p < 0.001$) and a smaller bone-surface-to-volume ratio (BS/BV; $p < 0.001$) than trabecular bone. Apparent mechanical properties

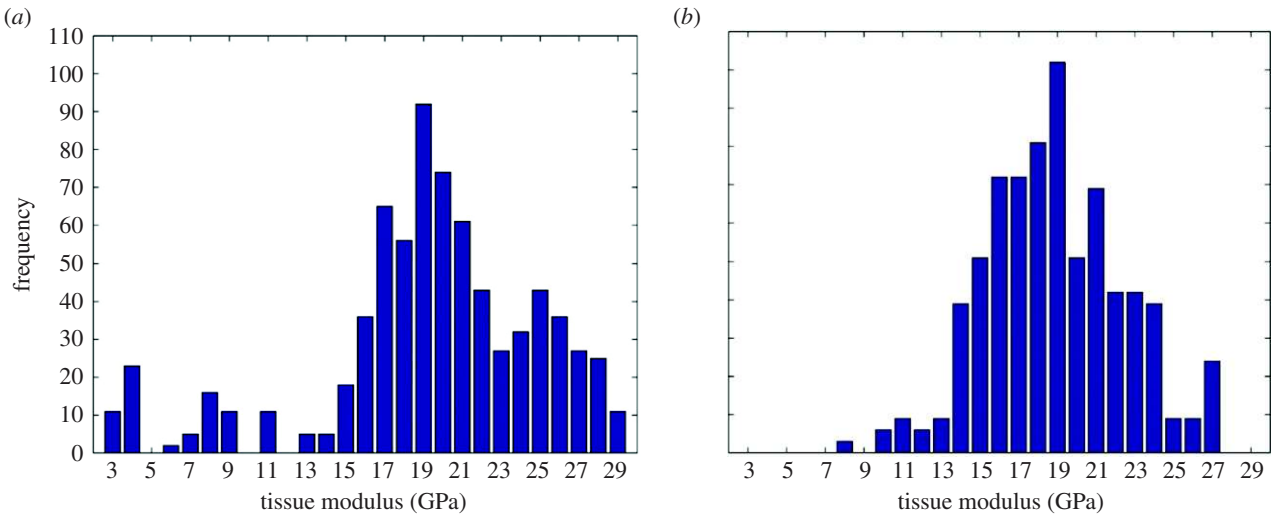

Figure 6. Tissue modulus frequency plots. (*a*) Cortical bone; (*b*) trabecular bone. (Online version in colour.)

showed that the cortical bone modulus of elasticity (E) and yield strength (YS) values were approximately four times greater than those of trabecular bone ($p < 0.001$ for both cases). Both bone types failed at the segment of the smallest cross section (table 4).

At the nanostructural level, no significant differences in tissue modulus and hardness were observed between the two bone types ($p = 0.46$ and 0.72, respectively; table 4). Cortical bone demonstrated higher modulus variability than trabecular bone (standard deviation was 5.73 GPa for cortical bone and 3.77 GPa for trabecular bone; figure 6). Amino acid analysis indicated no differences in total protein and collagen levels between the two bone types ($p = 0.59$ and 0.90, respectively). However, collagen content in cortical specimens was on average 7% greater than that of trabecular bone specimens ($p < 0.001$, table 4).

Non-apatitic phosphate (PO_4^{-3}) content did not differ between groups ($p = 0.25$), neither did the HPO_4 content in the hydrated surface layer ($p = 0.44$). Carbonate (CO_3) content also showed no difference among trabecular and cortical specimens ($p = 0.01$).

There were no differences between groups in carbonate-to-phosphate (C/P) and protein-to-mineral ratios ($p = 0.09$ and 0.89, respectively). Additionally, there were no differences in calcium and phosphate contents of the two bone types ($p = 0.29$ and 0.76, respectively; table 4).

The mathematical model's validation is based on elastic moduli values obtained during mechanical testing (table 3). The R^2 between the experimental and modelling axial stiffness values is 0.82, which shows relatively high agreement between the results (figure 7). The average values of axial elastic modulus (C_{33}) found from micromechanics modelling for cortical and trabecular bone are 8.40 and 3.02 GPa, respectively. Experimental results show these values to be 8.34 and 2.85 GPa for cortical and trabecular bone, respectively. Based on the continuum micromechanics approach, the elastic tensor for rat cortical and trabecular bone can be evaluated as

$$\mathbf{C}_{\text{cortical}} = \begin{bmatrix} 5.78 & 3.12 & 3.31 & 0 & 0 & 0 \\ 3.12 & 5.78 & 3.31 & 0 & 0 & 0 \\ 3.31 & 3.31 & 8.40 & 0 & 0 & 0 \\ 0 & 0 & 0 & 4.04 & 0 & 0 \\ 0 & 0 & 0 & 0 & 4.04 & 0 \\ 0 & 0 & 0 & 0 & 0 & 2.88 \end{bmatrix} \quad (3.1)$$

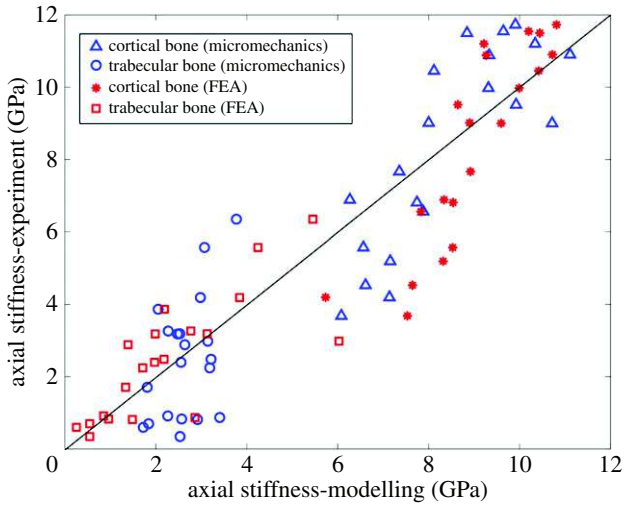

Figure 7. Comparison of axial elastic stiffness between micromechanics modelling and finite-element modelling with experiments for cortical and trabecular bone. FEA, finite-element analysis. (Online version in colour.)

and

$$\mathbf{C}_{\text{trabecular}} = \begin{bmatrix} 1.98 & 1.06 & 1.15 & 0 & 0 & 0 \\ 1.06 & 1.98 & 1.15 & 0 & 0 & 0 \\ 1.15 & 1.15 & 2.85 & 0 & 0 & 0 \\ 0 & 0 & 0 & 1.34 & 0 & 0 \\ 0 & 0 & 0 & 0 & 1.34 & 0 \\ 0 & 0 & 0 & 0 & 0 & 0.94 \end{bmatrix}. \quad (3.2)$$

Axial displacement contours of cortical and trabecular bone samples were obtained using finite-element analysis, as shown in figure 8. The axial displacement contour distribution in cortical bone is more regular than that in trabecular bone. The elastic moduli derived from finite-element analysis are shown in figure 7. There was a strong correlation between finite-element analysis results and mechanical testing results ($R^2 = 0.84$).

4. Discussion

The aim of this study was to explore the hierarchical nature of the two major bone types in rats. By using a variety of

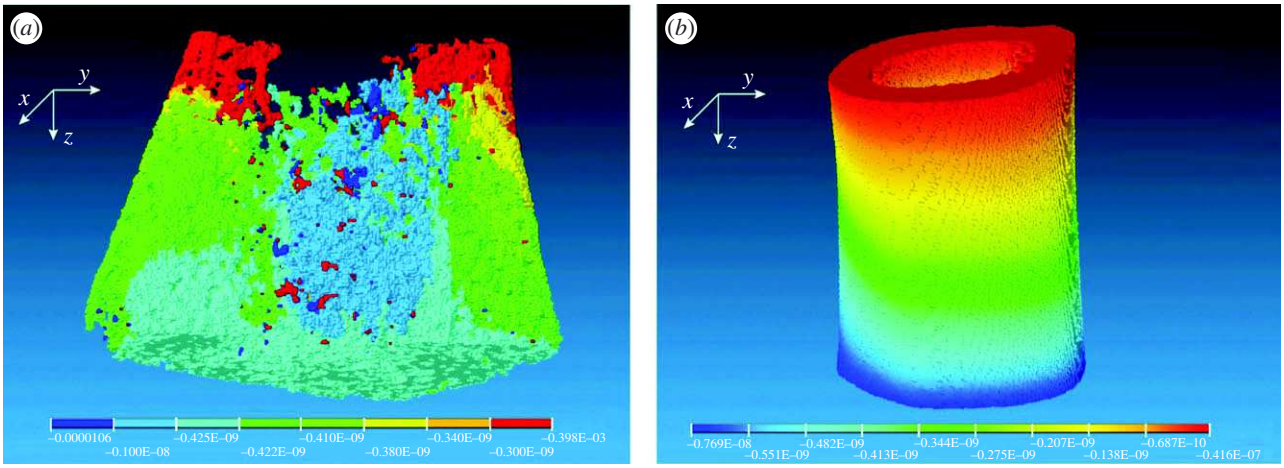

Figure 8. Axial displacement contours of (*a*) trabecular bone and (*b*) cortical bone obtained from finite element analysis.

analytical techniques, we were able to characterize the structural and compositional properties of cortical and trabecular bone, as well as to determine the best mathematical model to predict the tissue's mechanical properties.

Our hierarchical analysis demonstrated that the differences between cortical and trabecular bone reside mainly at the micro- and macrostructural levels. Our findings are consistent with those of previous studies: modulus of elasticity and yield strength values were significantly lower in trabecular bone specimens [7,24,26,27,29,30]. Although not evidenced in our study, Choi & Goldstein [7] made the same asseveration, emphasizing the higher mineral density values seen in trabecular bone. These findings can be explained by the configuration of lamellar/collagen fibres within the tissue, along with other microstructural characteristics that altogether support the fact that tissue morphology, and not just mineral density, plays a major role in determining the mechanical properties of cortical bone. The wide range of apparent elastic moduli can be explained by the wide range of bone volume fraction in the samples. Another factor causing the high degree of dispersion could be the way of calculating the apparent modulus: the resultant force is divided by the minimum cross-section area to determine the apparent elastic modulus (figure 3). Therefore, some of the apparent elastic moduli for trabecular bone are larger than those of cortical bone.

As shown by previous studies that also used FT-IR, carbonate content is significantly greater in cortical bone [13]. This finding may be explained by the critical role played by this ion during mineralization, coupled to the fact that cortical bone undergoes less remodelling over time. Khun *et al.* [11] described the differences in the mineral content and crystal maturation process in young and old animals, which mirror those seen in cortical and trabecular bone, respectively. For this reason, the differences between the mineral crystals may be attributed to their age, as well as to contrasting extents of post-translational modifications in the collagen structure [12,13,19,81]. The higher protein-to-mineral ratio and collagen content in protein seen in cortical bone seems to be similarly linked to its mechanical properties. The intermolecular cross-linking of collagen strongly determines the way fibrils are arranged to ultimately provide matrices with tensile strength and viscoelasticity [82,83]. Although a weak trend was evidenced in the carbonate-to-phosphate ratio between bone types, this finding further demonstrates the reigning similarities of cortical and trabecular bone at the compositional level.

Analysis performed at the nanostructural level yielded results that were consistent with previous reports in the literature, where hardness is basically considered to be similar between both bone types [19,25,32]. Hodgskinson *et al.* [19] described a strong relationship between calcium content and hardness, all equally similar across specimens compared in this study.

The purpose of mathematical modelling was to predict the bone's mechanical properties (i.e. anisotropic elastic moduli) as a function of the elementary components of the bone. For mathematical modelling, two approaches have been proposed in the literature for attributing the anisotropy to the bone structure, namely 'mineral-reinforced collagen matrix' [84–86] and 'collagen-reinforced mineral matrix' [71,87,88]. Both these approaches have been incorporated in the proposed model; the choice of platelet-shaped HA as an inclusion imposes anisotropy at the nanoscale and the choice of cylindrical-shaped collagen molecules as an inclusion imposes anisotropy at the submicroscale (figure 5). Regarding the shape of the elementary constituents of bone, it has been shown that HA crystals have plate-like shapes [89]. In this study, the HA crystals are assumed to be plate-like, which affects the Eshelby tensor and eventually the micromechanics model. Other approaches have employed spherical shapes to model HA inclusions [41]. The results of mathematical modelling are highly dependent on the choice of the mechanical properties of bone elementary components (i.e. HA and collagen). Here, we used the data from Katz & Ukraincik [72] and Yang *et al.* [73] for HA and collagen, respectively. These values also have been used by Hellmich & Ulm [71] and Hamed *et al.* [90] for multi-scale modelling of bone, and the results have shown good agreement with experimental findings. As seen in figure 7, finite-element modelling results better correlate with the mechanical testing results, especially for trabecular bone samples ($R^2 = 0.56$ for finite-element modelling versus $R^2 = 0.2$ for micromechanics modelling). The reason is that micromechanics modelling provides more crude results, as the bone structure become more disorganized.

For comparison, bone mineral, organic and water densities and bone volume fractions of the samples are plotted along with the results of other organs and species in the literature [21,79,91–97] (figure 9). These plots were first reported by Vuong & Hellmich [97] to verify the universal relation among the bone constituents. As outlined in Vuong & Hellmich [97],

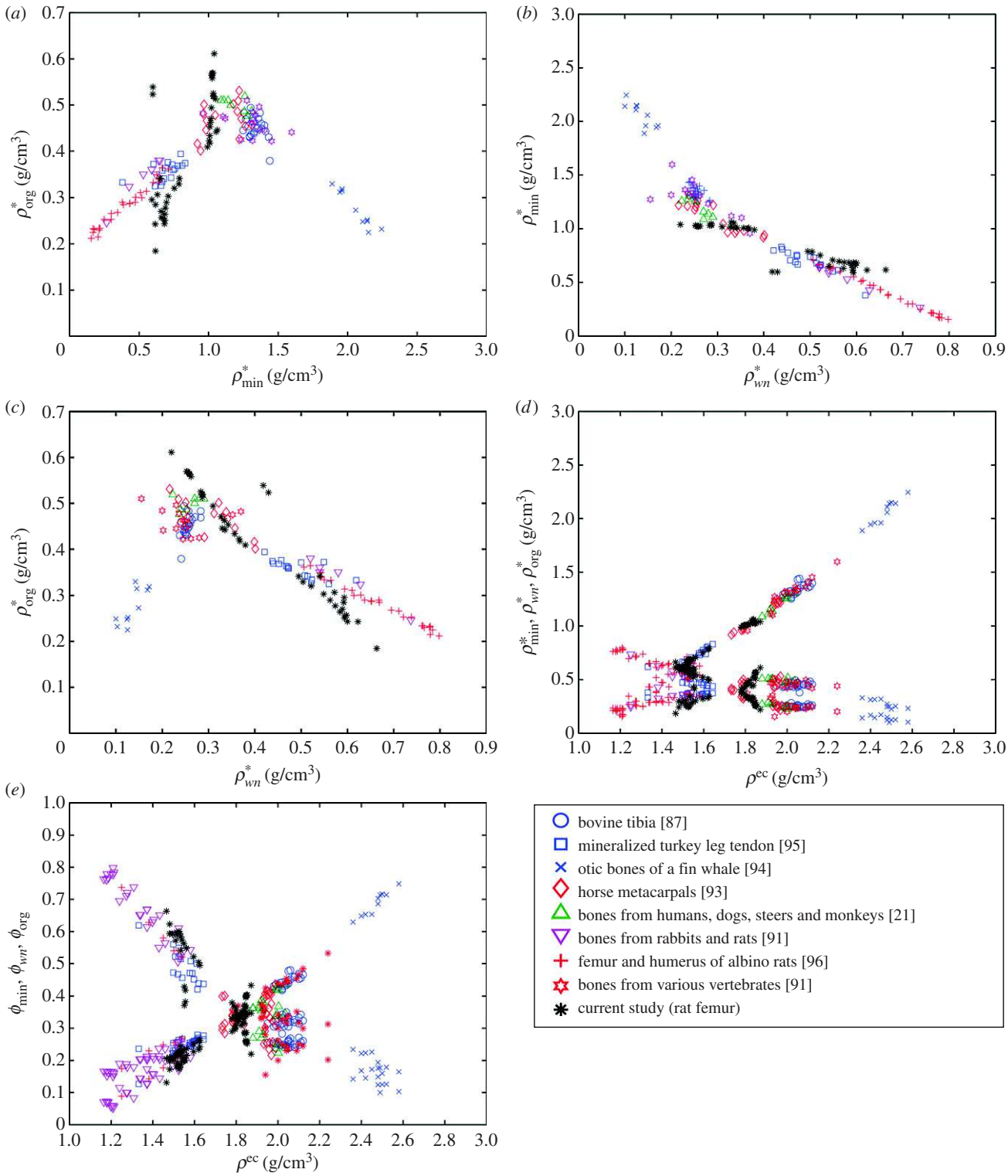

Figure 9. Relation between (*a*) apparent mineral (ρ^*_{min}) and organic (ρ^*_{org}) densities, (*b*) apparent water and non-collagenous proteins (ρ^*_{wn}) and mineral (ρ^*_{min}) densities, (*c*) apparent water and non-collagenous proteins (ρ^*_{wn}) and mineral (ρ^*_{org}) densities, (*d*) apparent densities and (*e*) volume fractions of mineral (ρ^*_{min}, ϕ_{min}), organic (ρ^*_{org}, ϕ_{org}) and water and non-collagenous proteins (ρ^*_{wn}, ϕ_{wn}) versus extracellular bone density (ρ^{ec}).

these figures can be divided into two regions and be presented by bilinear functions. Figure 9*a–c* is plotted based on mineral (ρ^*_{min}), organic (ρ^*_{org}) and water and non-collagenous protein (ρ^*_{wn}) densities. Alternatively, extracellular bone density can be found as

$$\rho^{ec} = \rho^*_{min} + \rho^*_{org} + \rho^*_{wn}. \tag{3.3}$$

Densities of bone composition elements (ρ^*_{min}, ρ^*_{org} and ρ^*_{wn}) are plotted versus extracellular bone density in figure 9*d*. The volume fractions of bone constituents (ϕ_{min}, ϕ_{org} and ϕ_{wn}) versus extracellular bone density are shown in figure 9*e*. In figure 9*a*, in the region with positive slope, the organic density (ρ^*_{org}) is increased by increasing extracellular bone mineral density (ρ^*_{min}). This region is represented by growing organisms and species, whereas the region with negative slope represents the adult organisms [97]. Figure 9*a–e* shows that the reported results in this study for bone composition densities and volume fractions are comparable to previous studies in the literature. In addition, our results further validate

the universal relation between different bone composition elements [97].

In this study, we did not consider the potential differences in geometry in the two bone types being compared. We strongly believe that it would be relevant to address the roles of lacunae and osteons in the structural properties of trabecular and cortical bone. In addition, the inferior resolution of FT-IR at very small scales introduces another limitation to our study [18]. In spite of these shortcomings, this study provides a comprehensive framework for trabecular and cortical bone properties that can be expanded upon in future studies.

Acknowledgements. The authors acknowledge the late Dr Melvin Glimcher from Boston Children's Hospital for his guidance throughout the project. They also acknowledge Dr Eugene Eckstein from the University of Memphis for providing support with the nanoindentation analysis component of the study.

Funding statement. This work was supported in part by the Qatar National Research Foundation (QNRF; NPRP 5-086-2-031) and departmental funding from the Children's Hospital Orthopaedic Surgery Foundation.

Appendix A

A.1. P-tensor in a transversely isotropic matrix

For a detailed derivation of the **P**-tensor for anisotropic matrices, please refer to [70,98]. For a transversely isotropic material, the non-zero terms of the stiffness matrix **C** are $C_{11} = C_{22}, C_{33}, C_{12}, C_{13} = C_{23}, C_{44} = C_{55}$ and $C_{66} = 1/2(C_{11} - C_{22})$. For spherical inclusions, the non-zero terms of the P-tensor can be found as

$$\begin{aligned} P_{11} = \frac{1}{16}\int_{-1}^{1} ((&2C_{13}^2 - 6C_{44}^2 - 5C_{11}C_{33} + 3C_{12}C_{33} + 5C_{11}C_{44} \\ &- 3C_{12}C_{44} + 8C_{33}C_{44})x^6 + (6C_{44} - 4C_{13}^2 + 6C_{44}^2 + 5C_{11}C_{33} \\ &- 6C_{12}C_{33} - 15C_{11}C_{44} + 9C_{12}C_{44} - 8C_{33}C_{44})x^4 + 5C_{11}^2C_{33}x^3 \\ &+ (2C_{13}^2 - 6C_{44} + 3C_{12}C_{33} + 15C_{11}C_{44} - 9C_{12}C_{44})x^2 \\ &- 5C_{11}^2C_{33}x + 3C_{12}C_{44} - 5C_{11}C_{44})(x^2 - 1)/D1\,\mathrm{d}x, \end{aligned} \tag{A1}$$

$$\begin{aligned} P_{12} = \frac{1}{16}\int_{-1}^{1} ((&2C_{13} - 2C_{44}^2 - C_{11}C_{33} - C_{12}C_{33} + C_{11}C_{44} + C_{12}C_{44} \\ &+ 4C_{13}C_{44})x^6 + (2C_{11}C_{33} - 2C_{13}^2 - 4C_{44}^2 - 2C_{13} + 2C_{12}C_{33} \\ &- 3C_{11}C_{44} - 3C_{12}C_{44} - 8C_{13}C_{44})x^4 + (2C_{13}^2 + 2C_{44}^2 \\ &- C_{11}C_{33} - C_{12}C_{33} + 3C_{11}C_{44} + 3C_{12}C_{44} + 4C_{13}C_{44})x^2 \\ &- C_{11}C_{44} - C_{12}C_{44})/D1\,\mathrm{d}x, \end{aligned} \tag{A2}$$

$$P_{13} = \frac{1}{4}\int_{-1}^{1} ((C_{13} + C_{44})x^4 + (-C_{13} - C_{44})x^2)/D2\,\mathrm{d}x\,, \tag{A3}$$

$$\begin{aligned} P_{44} = \frac{1}{16}\int_{-1}^{1} ((&2C_{13}^2 - C_{11}^2 + C_{11}C_{12} - 2C_{11}C_{13} + 2C_{12}C_{13} - 3C_{11}C_{33} \\ &+ C_{12}C_{33} + 4C_{11}C_{44} + 8C_{13}C_{44} + 4C_{33}C_{44})x^6 \\ &+ (3C_{11}^2 - 2C_{13}^2 - 3C_{11}C_{12} + 4C_{11}C_{13} - 4C_{12}C_{13} - C_{12}C_{33} \\ &- 5C_{11}C_{44} - 8C_{13}C_{44})x^4 + (3C_{11}C_{12} - 3C_{11}^2 \\ &- 2C_{11}C_{13} + 2C_{12}C_{13} + 4C_{11}C_{44})x^2 \\ &+ C_{11}^2 - C_{12}C_{11})/D1dx \end{aligned} \tag{A4}$$

and

$$P_{33} = \frac{1}{2}\int_{-1}^{1} ((C_{44} - C_{11})x^4 + C_{11}x^2)/D2\,\mathrm{dx}, \tag{A5}$$

where

$$\begin{aligned} D1 = (&C_{12}C_{13}^2 + C_{11}^2C_{33} + 2C_{11}C_{44}^2 - C_{11}^2C_{44} + 4C_{13}C_{44}^2 \\ &+ 2C_{33}C_{44}^2 - C_{11}C_{13} + 2C_{13}C_{44} - C_{11}C_{12}C_{33} + C_{11}C_{12}C_{44} \\ &- 2C_{11}C_{13}C_{44} + 2C_{12}C_{13}C_{44} - 3C_{11}C_{33}C_{44} + C_{12}C_{33}C_{44})x^6 \\ &+ (2C_{11}C_{13} - 2C_{11}^2C_{33} - 4C_{11}C_{44}^2 - 4C_{13}C_{44}^2 - 2C_{13}^2C_{44} \\ &- 2C_{12}C_{13}^2 + 3C_{11}C_{44} + 2C_{11}C_{12}C_{33} + 4C_{11}C_{13}C_{44} \\ &- 4C_{12}C_{13}C_{44} + 3C_{11}C_{33}C_{44} - C_{12}C_{33}C_{44})x^4 \\ &+ (C_{12}C_{13}^2 - C_{11}C_{13}^2 + C_{11}^2C_{33} + 2C_{11}C_{44}^2 - 3C_{11}^2C_{44} - 2C_{11}C_{44} \\ &- C_{11}C_{12}C_{33} + 3C_{11}C_{12}C_{44} + 2C_{12}C_{13}C_{44})x^2 \\ &+ C_{44}C_{11}^2 - 4C_{12}C_{44}C_{11} \end{aligned} \tag{A6}$$

and

$$\begin{aligned} D2 = (&C_{13}^2 + 2C_{44}C_{13} + C_{11}C_{44} + C_{33}C_{44})x^4 + (-C_{13}^2 \\ &- 2C_{44}C_{13} + C_{11}C_{33} - 2C_{11}C_{44})x^2 + C_{11}C_{44} \\ &- C_{11}C_{33}. \end{aligned} \tag{A7}$$

For cylindrical inclusions, the non-zero terms of the **P**-tensor are written as

$$P_{11} = P_{22} = P_{66} = \frac{1/8(5C_{11} - 3C_{12})}{C_{11}(C_{11} - C_{12})}, \tag{A8}$$

$$P_{12} = \frac{-1/8(C_{11} + C_{12})}{C_{11}(C_{11} - C_{12})} \tag{A9}$$

and

$$P_{44} = P_{55} = \frac{1}{8C_{44}}. \tag{A10}$$

For platelet-shape-like inclusions the **P**-tensor becomes

$$P_{33} = \frac{1}{C_{33}}. \tag{A11}$$

A.2. P-tensor in an isotropic matrix

For isotropic material, the stiffness matrix can be written as $\boldsymbol{C} = 3k\mathbf{I}^{\mathrm{vol}} + 2\mu\mathbf{I}^{\mathrm{dev}}$, where k and μ are the bulk and shear modulus, respectively, and $\mathbf{I}^{\mathrm{vol}}$ and $\mathbf{I}^{\mathrm{dev}}$ are the volumetric and deviatoric part of the fourth-order unity tensor ($\mathbf{I}^{\mathrm{vol}} = 1/3\delta_{ij}\delta_{kl}$ and $\mathbf{I}^{\mathrm{dev}} = \mathbf{I} - \mathbf{I}^{\mathrm{vol}}$). The **P**-tensor in an isotropic matrix for cylindrical inclusions can be written as [45,98]

$$\boldsymbol{P}_{\mathrm{cyl}} = \boldsymbol{S}_{\mathrm{cyl}}^{\mathrm{Esh}} : \boldsymbol{C}^{-1}, \tag{A12}$$

where the Eshelby tensor has the following non-zero terms:

$$S_{11}^{\mathrm{Esh}} = S_{22}^{\mathrm{Esh}} = \frac{9/4(k + \mu)}{(3k + 4\mu)}, \tag{A13}$$

$$S_{12}^{\mathrm{Esh}} = \frac{1/4(3k - 5\mu)}{(3k + 4\mu)}, \tag{A14}$$

$$S_{13}^{\mathrm{Esh}} = S_{23}^{\mathrm{Esh}} = \frac{1/2(3k - 2\mu)}{(3k + 4\mu)}, \tag{A15}$$

$$S_{44}^{\mathrm{Esh}} = S_{55}^{\mathrm{Esh}} = \frac{1}{4} \tag{A16}$$

and

$$S_{66}^{\mathrm{Esh}} = \frac{1/4(3k + 7\mu)}{(3k + 4\mu)}. \tag{A17}$$

References

1. Aerssens J, Boonen S, Joly J, Dequeker J. 1997 Variations in trabecular bone composition with anatomical site and age: potential implications for bone quality assessment. *J. Endocrinol.* **155**, 411–421. (doi:10.1677/joe.0.1550411)
2. Clarke B. 2008 Normal bone anatomy and physiology. *Clin. J. Am. Soc. Nephrol.* **3**(Suppl. 3), S131–S139. (doi:10.2215/CJN.04151206)
3. Oftadeh R, Perez-Viloria M, Villa-Camacho JC, Vaziri A, Nazarian A. 2015 Biomechanics and mechanobiology of trabecular bone: a review. *J. Biomech. Eng.* **137**, 010802. (doi:10.1115/1.4029176)
4. Zysset PK, Guo XE, Hoffler CE, Moore KE, Goldstein SA. 1999 Elastic modulus and hardness of cortical and trabecular bone lamellae measured by nanoindentation in the human femur. *J. Biomech.* **32**, 1005–1012. (doi:10.1016/S0021-9290(99)00111-6)
5. Wiberg G. 1939 Studies on dysplastic acetabula and congenital subluxation of the hip joint with special reference to the complication of osteoarthritis. *Acta Chir. Scand.* **58**, 1–135.
6. Spadaro JA, Werner FW, Brenner RA, Fortino MD, Fay LA, Edwards WT. 1994 Cortical and trabecular bone contribute strength to the osteopenic distal radius. *J. Orthop. Res.* **12**, 211–218. (doi:10.1002/jor.1100120210)
7. Choi K, Goldstein SA. 1992 A comparison of the fatigue behavior of human trabecular and cortical bone tissue. *J. Biomech.* **25**, 1371–1381. (doi:10.1016/0021-9290(92)90051-2)
8. Cauley JA, Blackwell T, Zmuda JM, Fullman RL, Ensrud KE, Stone KL, Barrett-Connor E, Orwoll ES. 2010 Correlates of trabecular and cortical volumetric bone mineral density at the femoral neck and lumbar spine: the osteoporotic fractures in men study (MrOS). *J. Bone Miner Res.* **25**, 1958–1971. (doi:10.1002/jbmr.86)
9. Barbour KE *et al*. 2010 Correlates of trabecular and cortical volumetric bone mineral density of the radius and tibia in older men: the osteoporotic fractures in men study. *J. Bone Miner. Res.* **25**, 1017–1028. (doi:10.1002/jbmr.6)
10. Lehtinen JT, Tingart MJ, Apreleva M, Warner JJ. 2004 Total, trabecular, and cortical bone mineral density in different regions of the glenoid. *J. Shoulder Elbow Surg.* **13**, 344–348. (doi:10.1016/S1058274604000291)
11. Kuhn LT, Grynpas MD, Rey CC, Wu Y, Ackerman JL, Glimcher MJ. 2008 A comparison of the physical and chemical differences between cancellous and cortical bovine bone mineral at two ages. *Calcif. Tissue Int.* **83**, 146–154. (doi:10.1007/s00223-008-9164-z)
12. Suarez KN, Romanello M, Bettica P, Moro L. 1996 Collagen type I of rat cortical and trabecular bone differs in the extent of posttranslational modifications. *Calcif. Tissue Int.* **58**, 65–69. (doi:10.1007/BF02509548)
13. Bigi A, Cojazzi G, Panzavolta S, Ripamonti A, Roveri N, Romanello M, Noris Suarez K, Moro L. 1997 Chemical and structural characterization of the mineral phase from cortical and trabecular bone. *J. Inorg. Biochem.* **68**, 45–51. (doi:10.1016/S0162-0134(97)00007-X)
14. Laib A, Barou O, Vico L, Lafage-Proust MH, Alexandre C, Rugsegger P. 2000 3D micro-computed tomography of trabecular and cortical bone architecture with application to a rat model of immobilisation osteoporosis. *Med. Biol. Eng. Comput.* **38**, 326–332. (doi:10.1007/BF02347054)
15. Bagi CM, Hanson N, Andresen C, Pero R, Lariviere R, Turner CH, Laib A. 2006 The use of micro-CT to evaluate cortical bone geometry and strength in nude rats: correlation with mechanical testing, pQCT and DXA. *Bone* **38**, 136–144. (doi:10.1016/j.bone.2005.07.028)
16. Boskey AL, Moore DJ, Amling M, Canalis E, Delany AM. 2003 Infrared analysis of the mineral and matrix in bones of osteonectin-null mice and their wildtype controls. *J. Bone Miner. Res.* **18**, 1005–1011. (doi:10.1359/jbmr.2003.18.6.1005)
17. Verdelis K *et al*. 2008 DSPP effects on *in vivo* bone mineralization. *Bone* **43**, 983–990. (doi:10.1016/j.bone.2008.08.110)
18. Goodyear SR, Gibson IR, Skakle JM, Wells RP, Aspden RM. 2009 A comparison of cortical and trabecular bone from C57 Black 6 mice using Raman spectroscopy. *Bone* **44**, 899–907. (doi:10.1016/j.bone.2009.01.008)
19. Hodgskinson R, Currey JD, Evans GP. 1989 Hardness, an indicator of the mechanical competence of cancellous bone. *J. Orthop. Res.* **7**, 754–758. (doi:10.1002/jor.1100070518)
20. Mulder L, van Ruijven LJ, Koolstra JH, van Eijden TM. 2007 Biomechanical consequences of developmental changes in trabecular architecture and mineralization of the pig mandibular condyle. *J. Biomech.* **40**, 1575–1582. (doi:10.1016/j.jbiomech.2006.07.030)
21. Gong JK, Arnold JS, Cohn SH. 1964 Composition of trabecular and cortical bone. *Anat. Rec.* **149**, 325–331. (doi:10.1002/ar.1091490303)
22. Norrdin RW, Phemister RD, Jaenke RS, Lo Presti CA. 1977 Density and composition of trabecular and cortical bone in perinatally irradiated beagles with chronic renal failure. *Calcif. Tissue Res.* **24**, 99–104. (doi:10.1007/BF02223302)
23. Dyson ED, Whitehouse WJ. 1968 Composition of trabecular bone in children and its relation to radiation dosimetry. *Nature* **217**, 576–578. (doi:10.1038/217576a0)
24. Guo XE, Goldstein SA. 1998 Is trabecular bone tissue different from cortical bone tissue? *Forma* **12**, 185–196.
25. Rho JY, Tsui TY, Pharr GM. 1997 Elastic properties of human cortical and trabecular lamellar bone measured by nanoindentation. *Biomaterials* **18**, 1325–1330. (doi:10.1016/S0142-9612(97)00073-2)
26. Turner CH, Rho J, Takano Y, Tsui TY, Pharr GM. 1999 The elastic properties of trabecular and cortical bone tissues are similar: results from two microscopic measurement techniques. *J. Biomech.* **32**, 437–441. (doi:10.1016/S0021-9290(98)00177-8)
27. Bayraktar HH, Morgan EF, Niebur GL, Morris GE, Wong EK, Keaveny TM. 2004 Comparison of the elastic and yield properties of human femoral trabecular and cortical bone tissue. *J. Biomech.* **37**, 27–35. (doi:10.1016/S0021-9290(03)00257-4)
28. Pollock NK, Laing EM, Taylor RG, Baile CA, Hamrick MW, Hall DB, Lewis RD. 2011 Comparisons of trabecular and cortical bone in late adolescent black and white females. *J. Bone Miner. Metab.* **29**, 44–53. (doi:10.1007/s00774-010-0186-z)
29. Choi K, Kuhn JL, Ciarelli MJ, Goldstein SA. 1990 The elastic moduli of human subchondral, trabecular, and cortical bone tissue and the size-dependency of cortical bone modulus. *J. Biomech.* **23**, 1103–1113. (doi:10.1016/0021-9290(90)90003-L)
30. Kuhn JL, Goldstein SA, Choi K, London M, Feldkamp LA, Matthews LS. 1989 Comparison of the trabecular and cortical tissue moduli from human iliac crests. *J. Orthop. Res.* **7**, 876–884. (doi:10.1002/jor.1100070614)
31. Toolan B, Shea M, Myers E, Borchers R, Seedor J, Quartuccio H, Rodan G, Hayes W. 1992 Effects of 4-amino-1-hydroxybutylidene bisphosphonate on bone biomechanics in rats. *J. Bone Miner. Res.* **7**, 1399–1406. (doi:10.1002/jbmr.5650071207)
32. Ko C-C, Douglas WH, Cheng Y-S. 1995 Intrinsic mechanical competence of cortical and trabecular bone measured by nanoindentation and microindentation probes. *ASME-Publ. BED* **29**, 415.
33. Martin RB, Ishida J. 1989 The relative effects of collagen fiber orientation, porosity, density, and mineralization on bone strength. *J. Biomech.* **22**, 419–426. (doi:10.1016/0021-9290(89)90202-9)
34. Kotha SP, Guzelsu N. 2007 Tensile behavior of cortical bone: dependence of organic matrix material properties on bone mineral content. *J. Biomech.* **40**, 36–45. (doi:10.1016/j.jbiomech.2005.11.016)
35. Currey JD. 1988 The effect of porosity and mineral content on the Young's modulus of elasticity of compact bone. *J. Biomech.* **21**, 131–139. (doi:10.1016/0021-9290(88)90006-1)
36. Boskey AL, Wright TM, Blank RD. 1999 Collagen and bone strength. *J. Bone Miner. Res.* **14**, 330–335. (doi:10.1359/jbmr.1999.14.3.330)
37. Hernandez CJ, Beaupre GS, Keller TS, Carter DR. 2001 The influence of bone volume fraction and ash fraction on bone strength and modulus. *Bone* **29**, 74–78. (doi:10.1016/S8756-3282(01)00467-7)
38. Nikolov S, Raabe D. 2008 Hierarchical modeling of the elastic properties of bone at submicron scales: the role of extrafibrillar mineralization. *Biophys. J.* **94**, 4220–4232. (doi:10.1529/biophysj.107.125567)

39. Martínez-Reina J, Domínguez J, García-Aznar J. 2011 Effect of porosity and mineral content on the elastic constants of cortical bone: a multiscale approach. *Biomech. Model. Mechanobiol.* **10**, 309–322. (doi:10.1007/s10237-010-0236-4)
40. Fritsch A, Hellmich C, Dormieux L. 2009 Ductile sliding between mineral crystals followed by rupture of collagen crosslinks: experimentally supported micromechanical explanation of bone strength. *J. Theor. Biol.* **260**, 230–252. (doi:10.1016/j.jtbi.2009.05.021)
41. Fritsch A, Hellmich C. 2007 'Universal'microstructural patterns in cortical and trabecular, extracellular and extravascular bone materials: micromechanics-based prediction of anisotropic elasticity. *J. Theor. Biol.* **244**, 597–620. (doi:10.1016/j.jtbi.2006.09.013)
42. Hamed E, Jasiuk I, Yoo A, Lee Y, Liszka T. 2012 Multi-scale modelling of elastic moduli of trabecular bone. *J. R. Soc. Interface* **9**, 1654–1673. (doi:10.1098/rsif.2011.0814)
43. Hellmich C, Ulm FJ, Dormieux L. 2004 Can the diverse elastic properties of trabecular and cortical bone be attributed to only a few tissue-independent phase properties and their interactions? Arguments from a multiscale approach. *Biomech. Model. Mechanobiol.* **2**, 219–238. (doi:10.1007/s10237-004-0040-0)
44. Zaoui A. 1997 Structural morphology and constitutive behaviour of microheterogeneous materials. In *Continuum micromechanics* (ed. P Suquet), pp. 291–347. New York, NY: Springer.
45. Zaoui A. 2002 Continuum micromechanics: survey. *J. Eng. Mech.* **128**, 808–816. (doi:10.1061/(ASCE)0733-9399(2002)128:8(808))
46. Mura T. 1987 *Micromechanics of defects in solids*. Berlin, Germany: Springer.
47. Drugan W, Willis J. 1996 A micromechanics-based nonlocal constitutive equation and estimates of representative volume element size for elastic composites. *J. Mech. Phys. Solids* **44**, 497–524. (doi:10.1016/0022-5096(96)00007-5)
48. Dunn M, Taya M. 1993 Micromechanics predictions of the effective electroelastic moduli of piezoelectric composites. *Int. J. Solids Struct.* **30**, 161–175. (doi:10.1016/0020-7683(93)90058-F)
49. Cory E, Nazarian A, Entezari V, Vartanians V, Muller R, Snyder BD. 2010 Compressive axial mechanical properties of rat bone as functions of bone volume fraction, apparent density and micro-CT based mineral density. *J. Biomech.* **43**, 953–960. (doi:10.1016/j.jbiomech.2009.10.047)
50. Rey C, Shimizu M, Collins B, Glimcher MJ. 1991 Resolution-enhanced Fourier transform infrared spectroscopy study of the environment of phosphate ion in the early deposits of a solid phase of calcium phosphate in bone and enamel and their evolution with age: 2. Investigations in the nu3PO_4 domain. *Calcif. Tissue Int.* **49**, 383–388. (doi:10.1007/BF02555847)
51. Rey C, Collins B, Goehl T, Dickson IR, Glimcher MJ. 1989 The carbonate environment in bone mineral: a resolution-enhanced fourier transform infrared spectroscopy study. *Calcif. Tissue Int.* **45**, 157–164. (doi:10.1007/BF02556059)
52. Pleshko NL, Boskey AL, Mendelsohn R. 1992 An infrared study of the interaction of polymethyl methacrylate with the protein and mineral components of bone. *J. Histochem. Cytochem.* **40**, 1413–1417. (doi:10.1177/40.9.1506677)
53. Wergedal JE, Baylink DJ. 1974 Electron microprobe measurements of bone mineralization rate *in vivo*. *Am. J. Physiol.* **226**, 345–352.
54. Obrant KJ, Odselius R. 1985 Electron microprobe investigation of calcium and phosphorus concentration in human bone trabeculae: both normal and in posttraumatic osteopenia. *Calcif. Tissue Int.* **37**, 117–120. (doi:10.1007/BF02554829)
55. Fiske CH, Subbarow Y. 1925 The colorimetric determination of phosphorus. *J. Biol. Chem.* **66**, 375–400.
56. Bartlett GR. 1959 Phosphorus assay in column chromatography. *J. Biol. Chem.* **234**, 466–468.
57. Stanton MG. 1968 Colorimetric determination of inorganic phosphate in the presence of biological material and adenosine triphosphate. *Anal. Biochem.* **22**, 27–34. (doi:10.1016/0003-2697(68)90255-8)
58. Katz JL, Yoon HS, Lipson S, Maharidge R, Meunier A, Christel P. 1984 The effects of remodeling on the elastic properties of bone. *Calcif. Tissue Int.* **36**, S31–S36. (doi:10.1007/BF02406131)
59. Weiner S, Wagner HD. 1998 The material bone: structure-mechanical function relations. *Annu. Rev. Mater. Sci.* **28**, 271–298. (doi:10.1146/annurev.matsci.28.1.271)
60. Eshelby JD. 1957 The determination of the elastic field of an ellipsoidal inclusion, and related problems. *Proc. R. Soc. Lond. A* **241**, 376–396. (doi:10.1098/rspa.1957.0133)
61. Mori T, Tanaka K. 1973 Average stress in matrix and average elastic energy of materials with misfitting inclusions. *Acta Metall.* **21**, 571–574. (doi:10.1016/0001-6160(73)90064-3)
62. Wakashima K, Tsukamoto H. 1991 Mean-field micromechanics model and its application to the analysis of thermomechanical behaviour of composite materials. *Mater. Sci. Eng. A* **146**, 291–316. (doi:10.1016/0921-5093(91)90284-T)
63. Hershey A. 1954 The elasticity of an isotropic aggregate of anisotropic cubic crystals. *J. Appl. Mech.* **21**, 226–240.
64. Hill R. 1963 Elastic properties of reinforced solids: some theoretical principles. *J. Mech. Phys. Solids* **11**, 357–372. (doi:10.1016/0022-5096(63)90036-X)
65. Eppell SJ, Tong W, Katz JL, Kuhn L, Glimcher MJ. 2001 Shape and size of isolated bone mineralites measured using atomic force microscopy. *J. Orthop. Res.* **19**, 1027–1034. (doi:10.1016/S0736-0266(01)00034-1)
66. Currey J. 1964 Three analogies to explain the mechanical properties of bone. *Biorheology* **2**, 1–10.
67. Arena MJS, McEwen F. 1996 Structural relations between bone as determined by high microscopic tomography. *Microsc. Res. Tech.* **33**, 192–202. (doi:10.1002/(SICI)1097-0029(19960201)33:2<192::AID-JEMT9>3.0.CO;2-V)
68. Weiner S, Arad T, Traub W. 1991 Crystal organization in rat bone lamellae. *FEBS Lett.* **285**, 49–54. (doi:10.1016/0014-5793(91)80722-F)
69. Laws N. 1977 The determination of stress and strain concentrations at an ellipsoidal inclusion in an anisotropic material. *J. Elast.* **7**, 91–97. (doi:10.1007/BF00041133)
70. Laws N. 1985 A note on penny-shaped cracks in transversely isotropic materials. *Mech. Mater.* **4**, 209–212. (doi:10.1016/0167-6636(85) 90017-1)
71. Hellmich C, Ulm F-J. 2002 Micromechanical model for ultrastructural stiffness of mineralized tissues. *J. Eng. Mech.* **128**, 898–908. (doi:10.1061/(ASCE)0733-9399(2002)128:8(898))
72. Katz J, Ukraincik K. 1971 On the anisotropic elastic properties of hydroxyapatite. *J. Biomech.* **4**, 221–227. (doi:10.1016/0021-9290(71)90007-8)
73. Yang L, van der Werf KO, Koopman BF, Subramaniam V, Bennink ML, Dijkstra PJ, Feijen J. 2007 Micromechanical bending of single collagen fibrils using atomic force microscopy. *J. Biomed. Mater. Res. A* **82**, 160–168. (doi:10.1002/jbm.a.31127)
74. Lees S. 1987 Considerations regarding the structure of the mammalian mineralized osteoid from viewpoint of the generalized packing model. *Connect. Tissue Res.* **16**, 281–303. (doi:10.3109/03008208709005616)
75. Katz EP, Li S-T. 1973 Structure and function of bone collagen fibrils. *J. Mol. Biol.* **80**, 1–15. (doi:10.1016/0022-2836(73)90230-1)
76. HM F. 1960 Measurement of osteocytes per unit volume and volume components of osteocytes and canaliculae in man. *Henry Ford Hospital Med. Bull.* **8**, 208–211.
77. Morris MA, Lopez-Curto JA, Hughes SP, An K-N, Bassingthwaighte JB, Kelly PJ. 1982 Fluid spaces in canine bone and marrow. *Microvasc. Res.* **23**, 188–200. (doi:10.1016/0026-2862(82)90064-4)
78. Cowin SC. 1999 Bone poroelasticity. *J. Biomech.* **32**, 217–238. (doi:10.1016/S0021-9290(98)00161-4)
79. Lees S, Cleary PF, Heeley JD, Gariepy EL. 1979 Distribution of sonic plesio-velocity in a compact bone sample. *J. Acoust. Soc. Am.* **66**, 641–646. (doi:10.1121/1.383689)
80. Sietsema W. 1995 Animal models of cortical porosity. *Bone* **17**, S297–S305.
81. Paschalis EP, Betts F, DiCarlo E, Mendelsohn R, Boskey AL. 1997 FTIR microspectroscopic analysis of normal human cortical and trabecular bone. *Calcif. Tissue Int.* **61**, 480–486. (doi:10.1007/s002239900371)
82. Paschalis EP, Shane E, Lyritis G, Skarantavos G, Mendelsohn R, Boskey AL. 2004 Bone fragility and collagen cross-links. *J. Bone Miner. Res.* **19**, 2000–2004. (doi:10.1359/JBMR.040820)
83. Yamauchi M, Woodley DT, Mechanic GL. 1988 Aging and cross-linking of skin collagen. *Biochem. Biophys. Res. Commun.* **152**, 898–903. (doi:10.1016/S0006-291X(88)80124-4)
84. Currey J. 1969 The relationship between the stiffness and the mineral content of bone.

J. Biomech. **2**, 477–480. (doi:10.1016/0021-9290(69)90023-2)
85. Katz JL. 1980 Anisotropy of Young's modulus of bone. *Nature* **283**, 106–107.
86. Jäger I, Fratzl P. 2000 Mineralized collagen fibrils: a mechanical model with a staggered arrangement of mineral particles. *Biophys. J.* **79**, 1737–1746. (doi:10.1016/S0006-3495(00)76426-5)
87. Lees S, Heeley JD, Cleary PF. 1979 A study of some properties of a sample of bovine cortical bone using ultrasound. *Calcif. Tissue Int.* **29**, 107–117. (doi:10.1007/BF02408065)
88. Hellmich C, Ulm F-J. 2002 Are mineralized tissues open crystal foams reinforced by crosslinked collagen? Some energy arguments. *J. Biomech.* **35**, 1199–1212. (doi:10.1016/S0021-9290(02)00080-5)
89. Yoon YJ, Cowin SC. 2008 The estimated elastic constants for a single bone osteonal lamella. *Biomech. Model. Mechanobiol.* **7**, 1–11. (doi:10.1007/s10237-006-0072-8)
90. Hamed E, Lee Y, Jasiuk I. 2010 Multiscale modeling of elastic properties of cortical bone. *Acta Mech.* **213**, 131–154. (doi:10.1007/s00707-010-0326-5)
91. Biltz RM, Pellegrino ED. 1969 The chemical anatomy of bone I. A comparative study of bone composition in sixteen vertebrates. *J. Bone Joint Surg.* **51**, 456–466.
92. Burns CM. 1929 The effect of the continued ingestion of mineral acid on growth of body and bone and on the composition of bone and of the soft tissues. *Biochem. J.* **23**, 860.
93. Lees S. 2003 Mineralization of type I collagen. *Biophys. J.* **85**, 204–207. (doi:10.1016/S0006-3495(03)74466-X)
94. Lees S, Hanson DB, Page EA. 1996 Some acoustical properties of the otic bones of a fin whale. *J. Acoust. Soc. Am.* **99**, 2421–2427. (doi:10.1121/1.415430)
95. Lees S, Page EA. 1992 A study of some properties of mineralized turkey leg tendon. *Connect. Tissue Res.* **28**, 263–287. (doi:10.3109/03008209209016820)
96. Hammett FS. 1925 A biochemical study of bone growth I. Changes in the ash, organic matter, and water during growth (mus norvegicus albinus). *J. Biol. Chem.* **64**, 409–428.
97. Vuong J, Hellmich C. 2011 Bone fibrillogenesis and mineralization: quantitative analysis and implications for tissue elasticity. *J. Theor. Biol.* **287**, 115–130. (doi:10.1016/j.jtbi.2011.07.028)
98. Hellmich C, Barthélémy J-F, Dormieux L. 2004 Mineral–collagen interactions in elasticity of bone ultrastructure–a continuum micromechanics approach. *Eur. J. Mech. A/Solids* **23**, 783–810. (doi:10.1016/j.euromechsol.2004.05.004)